

The Milky Way Bulge Extra-Tidal Star Survey: NGC 6569

1 JOANNE HUGHES,¹ ANDREA KUNDER,² KEVIN COVEY,³ KATHRYN DEVINE,⁴ KRISTEN A. LARSON,⁵
2 CARLOS CAMPOS,² ADRIAN M. PRICE-WHELAN,⁶ JOSEPH E. McEWEN,¹ GABRIEL PERREN,⁷
3 CHRISTIAN I. JOHNSON,⁸ CRAIG HORTON,¹ LUKE SMITH,¹ SARAH TORSET,¹ CYNTHIA LUNA,¹
4 MATTHEW KOLMANOVSKY,¹ FIONA KOVISTO,¹ LEANDER VILLARTA,¹ VY VUONG,¹ IULIA T. SIMION,⁹
5 KYLE WEBSTER,³ ERIKA SILVA,¹⁰ CATHERINE A. PILACHOWSKI,¹¹ MICHAEL RICH,¹²
6 JUSTIN A. KADER,¹³ ANDREAS J. KOCH-HANSEN,¹⁴ AND TOMMASO MARCHETTI¹⁴

7 ¹*Physics Department Seattle University, 901 12th Ave., Seattle, WA 98122, USA*

8 ²*Saint Martin's University, 5000 Abbey Way SE, Lacey, WA, 98503, USA*

9 ³*Department of Physics & Astronomy, Western Washington University, MS-9164, 516 High St., Bellingham, WA,
10 98225, USA*

11 ⁴*The College of Idaho, 2112 Cleveland Blvd Caldwell, ID, 83605, USA*

12 ⁵*National Solar Observatory, 3665 Discovery Dr, Boulder, CO, 80303, USA*

13 ⁶*Center for Computational Astrophysics, Flatiron Institute, 162 Fifth Ave., New York, 10010, NY, USA*

14 ⁷*Instituto de Astrofísica de La Plata, IALP (CONICETUNLP), 1900 La Plata, Argentina*

15 ⁸*Space Telescope Science Institute, 3700 San Martin Drive, Baltimore, MD 21218, USA*

16 ⁹*Shanghai Key Lab for Astrophysics, Shanghai Normal University, 100 Guilin Road, Shanghai, 200234*

17 ¹⁰*Fernbank Science Center, 156 Heaton Park Dr, Atlanta, GA 30307 156 Heaton Park Dr, Atlanta, GA, 30307, USA*

18 ¹¹*Indiana University Department of Astronomy, SW319, 727 E 3rd Street, Bloomington, IN 47405, USA*

19 ¹²*Department of Physics and Astronomy, UCLA, 430 Portola Plaza, Box 951547, Los Angeles, CA 90095-1547, USA*

20 ¹³*Department of Physics and Astronomy, 4129 Frederick Reines Hall, University of California, Irvine, CA 92697,
21 USA*

22 ¹⁴*European Southern Observatory, Karl-Schwarzschild-Strasse 2, 85748 Garching bei Munchen, Germany*

ABSTRACT

23 We present results from a spectroscopic survey to detect tidal debris associated with
24 the bulge globular cluster NGC 6569. Using Blanco-DECam Bulge Survey photometry
25 and Gaia proper motions, 305 candidate extra-tidal stars were identified, yielding 303

measurable spectra: 58 objects fell within NGC 6569’s radial velocity range of -25 to -65 km s^{-1} . We identified 41 potential extra-tidal stars and included 4 RR Lyrae stars in the cluster center. The 19 best candidates have radial velocities between -30 and -65 km s^{-1} , are located within 0.6 degrees of NGC 6569, with $[\text{Fe}/\text{H}] = -0.77 \pm 0.14$ dex and $[\alpha/\text{Fe}] = +0.27 \pm 0.12$ dex. Among the rejected candidates with similar proper motions to NGC 6569 but radial velocity and/or $[\text{Fe}/\text{H}]$ values outside those accepted for this system, there are 39 stars with $S/N > 35$ and another 21 have measurable α -enhancement, allowing us to deduce that their chemical characteristics are similar to the Fe- and α -abundances of other local bulge globular clusters, but additional kinematic modeling and higher resolution spectra are required to investigate their origins further.

Keywords: Stellar populations(1622) – Galactic archaeology(2178) – Milky Way dynamics (1051) – Galactic bulge(2041) – Galaxy bulges(578) – Globular star clusters(656) – (Galaxy:) Globular clusters: individual (NGC 6569)

1. INTRODUCTION

The physical, kinematic, and chemical properties of globular clusters (GCs) in the Milky Way (MW) provide valuable insight into Galactic potential, MW’s accretion history, and its early chemical evolution (Hozumi & Burkert 2015; de Boer et al. 2019; Piatti & Carballo-Bello 2020b), including the evolution of the Galactic bulge. This paper presents a new spectroscopic survey of NGC 6569, a massive GC located on the far side of the bulge. This is the third paper in the series and the first to address a massive GC. Previous studies include Kunder et al. (2024) on BH 261 and Butler et al. (2024) on RR Lyrae stars associated with Patchick 99. These studies are part of the “Milky Way Bulge extra-tidal star survey” (? , MWBest), a spectroscopic program to identify stars escaping from inner Galaxy clusters.

NGC 6569 is particularly interesting due to its potential tidal interactions with the surrounding environment. Despite being in the crowded and dusty bulge region, NGC 6569 remains distinct as a well-defined cluster, standing out against the surrounding stars and the highly variable extinction

53 in the area (see Fig. 1a). Previous studies have characterized the cluster's bound stellar population,
 54 simplifying the identification of stars outside its tidal radius of $\sim 6.9'$ (Valenti et al. 2011).

55 The central population of NGC 6569 has been extensively studied in surveys, including Hazen-Liller
 56 (1985); Ortolani et al. (2001); Valenti et al. (2005, 2011); Kunder et al. (2015); Johnson et al. (2018);
 57 Saracino et al. (2019); Pallanca et al. (2023). From now on, Johnson et al. (2018) will be referred
 58 to as J18, and (Pallanca et al. 2023) as P23. Johnson et al. (2020) suggest that NGC 6569's stellar
 59 population extends past the tidal radius. The results presented in our study extend to about five
 60 tidal radii around NGC 6569, aimed at identifying extra-tidal stars merging into the general field
 61 population of the bulge. The spectroscopic and kinematic studies of J18 and P23, which extend to
 62 the outer visible parts of the cluster, overlap with our extra-tidal selection within ≤ 2 tidal radii of
 63 the center of NGC 6569.

64 NGC 6569 is located at $R.A. = 18^h13^m38.3^s$ and $Dec. = -31^\circ49'35''$. Distance estimates range
 65 from 10.9 kpc (Harris 1996, 2010) to 10.1 kpc (Valenti et al. 2011). The Baumgardt et al. (2021)
 66 catalog (2021; Version 4 as of 2023) places the cluster at 10.530 ± 0.260 kpc using Gaia DR3 data
 67 and estimates its mass as $2.3 \times 10^5 M_\odot$ based on N-body simulations. The Gaia DR3 proper motions
 68 (PMs) centered on the cluster are $[-4.125, -7.354]$ mas/yr, and the average radial velocity (RV) is
 69 $-49.82 \pm 0.80 \text{ km s}^{-1}$. The cluster is estimated to be 13.0 Gyr old with $[\text{Fe}/\text{H}] = -0.75$ dex, fit with
 70 the MIST isochrones (this paper). Table 1 provides a summary of the relevant previous work, and
 71 Fig. 1a-c shows a pictorial description of the cluster environment, local Gaia DR3 PM, and distance
 72 estimates using the AStECA (Automated Stellar Cluster Analysis) Python code (Perren et al. 2015).

73 AStECA is used with the BDBS photometry combined with *Gaia* astrometry to estimate the general
 74 physical properties of the cluster to determine the probability of cluster membership for objects
 75 within the cluster radius (Fig.1d & e, & Fig.2a). AStECA is an excellent tool for finding the general
 76 properties of a cluster. AStECA utilizes a decontamination algorithm defining outlying fields but the
 77 code rejects stars outside the cluster radius. AStECA determines the center of the star cluster (open or
 78 globular), the stellar density profile, luminosity functions, completeness limits, and color-magnitude
 79 diagrams (CMDs). The solutions or the physical parameters derived from the King models (King

1962, 1966, Fig.1d) are detailed in Fig.1 and Table 1. The photometry was dereddened using the maps generated by Simion et al. (2017). The ASteca CMD fits use the PARSEC isochrones, which are solar-scaled (Bressan et al. 2012). Fits were also carried out with the MIST models, which can be α -enhanced (Choi et al. 2016).

The ASteca contamination index (CI) is a crucial metric used in the analysis of stellar clusters, particularly in distinguishing between true physical clusters and random overdensities of field stars. The contamination index quantifies the likelihood that a given star within the analyzed region belongs to the cluster (number of stars: n_{cl}) rather than being a field star (number of stars: n_{fl}).

$$CI = \frac{d_{field}}{n_{cl+fl}/A_{cl}} = \frac{n_{fl}}{n_{fl} + n_{cl}} \quad (1)$$

where d_{field} is the field star density over the total density of stars in the cluster region, A_{cl} is the area of the cluster, determined using the best King model fit to the data. Selecting objects with the PM limits, the contamination index is 0.35, meaning 35% of the stars within the cluster's radius were rejected as non-members. Only 529 ± 5 members are found using the King profile, and 538 ± 5 members are identified assuming a uniform background, above $G = 19$ mag. This membership identification is achieved through a Bayesian field star decontamination algorithm integrated into ASteca. The algorithm assigns membership probabilities to stars based on their photometric characteristics, allowing for a more accurate assessment of the cluster's true stellar population (Perren et al. 2015), and yields error estimates, with which empirical isochrone-fitting struggles. However, if there are tidal features present outside the cluster radius, this procedure might also skew the results and undercount the cluster membership.

From Table 1, the N-body fits from the Galactic Globular Cluster Database Version 4 (Baumgardt et al. 2021) are likely more accurate for the cluster mass due to the crowded field and dust, and the ASteca King model fits are consistent with their value for the distance to NGC 6569. Restricting the parallax (Plx) and PM from the Gaia catalog results in a shrinking of the estimate of the tidal radius compared to Valenti et al. (2011) and P23; Expanding the search area and not restricting the Plx and PM results in a higher estimated CI, and the cluster radius and tidal radius converging,

Table 1. NGC 6569: Physical Parameters & Model Fits

Distance	Mass	$\log_{10}[\text{Age}]$	Z or [Fe/H]	E(B-V)	r_{cl}	r_t	Note
kpc	$1 \times 10^5 M_\odot$	dex	dex	mag.	'	'	
10.530 ± 0.260	2.3	10.08	Z=0.008	0.49	2.7	6.9	[1]
10.1 ± 0.2	$1.72^{+0.20}_{-0.18}$	—	$[Fe/H] = -0.75, [\alpha/Fe] = +0.4$	—	—	$9.83^{+2.8}_{-1.8}$	[2]
$10.498^{+0.275}_{-0.273}$	—	—	—	—	$3.28^{+0.17}_{-0.20}$	$4.56^{+1.23}_{-0.53}$	[3]
$10.498^{+0.275}_{-0.273}$	—	—	—	—	$3.95^{+0.62}_{-0.68}$	$5.45^{+0.63}_{-0.50}$	[4]
10.8 ± 0.3	$4.9 \pm 0.4^*$	10.02 ± 0.02	$Z = 0.0081 \pm 0.0005$	0.49 ± 0.03	$5.2^{+0.6}_{-0.5}$	$4.8^{+0.4}_{-0.3}$	[5]
10.2 ± 0.3	$2.4 \pm 0.1^*$	10.00 ± 0.02	$Z = 0.0081 \pm 0.0003$	$0.027 \pm 0.003^{**}$	3.92 ± 0.01	5.50 ± 0.04	[6]
10.5 ± 0.3	—	10.08	$[Fe/H] = -0.75, [\alpha/Fe] = +0.3$	<i>Variable</i>	—	—	[7]

NOTE—[1] [Vasiliev & Baumgardt \(2021\)](#); [Baumgardt et al. \(2023\)](#); [Baumgardt et al. \(2021\)](#); [Baumgardt & Hilker \(2018\)](#); [Valenti et al. \(2011\)](#) - Galactic Globular Cluster Database Version 4, N-body fits, updated in 2023.

NOTE—[2] [Pallanca et al. \(2023\)](#); [Valenti et al. \(2011\)](#)

NOTE—[3] AStECA King model fit ([Perren et al. 2015](#); [King 1962, 1966](#)): Gaia Plx, PM, Gaia photometry for a radius of 0.5° from center, PM-restricted, no reddening correction.

NOTE—[4] AStECA King model fit ([Perren et al. 2015](#); [King 1962, 1966](#)): BDBS photometry (Gaia position match) for a radius of 0.5° , PM-restricted, no reddening correction.

NOTE—[5] AStECA fit ([Perren et al. 2015](#); [Bressan et al. 2012](#)): Gaia photometry for a radius of 1° , PM-restricted, no reddening correction, PARSEC isochrones.

NOTE—[6] AStECA fit ([Perren et al. 2015](#); [Bressan et al. 2012](#)): Averaging all BDBS colors, Gaia PM, radius of 0.5° , $Plx < 0.4$ mas limit, PM-restricted, reddening corrections applied, PARSEC isochrones.

NOTE—[7] Empirical CMD fit, dereddened by extinction map, MIST isochrones ([Simion et al. 2017](#); [Choi et al. 2016](#); [Valenti et al. 2011](#)).

*AStECA total initial mass using the [Kroupa \(2002\)](#) IMF. This is a lower limit mass limit because the code does not account for dynamical mass loss ([Perren et al. 2022](#)).

**Remaining extinction after removal according to the extinction map ([Kader et al. 2023](#)).

indicating that NGC 6569 should be dissolving ([Johnson et al. 2020](#)). GCs in the bulge of the MW are particularly vulnerable to tidal forces due to their proximity to the dense stellar environment and the gravitational influences of the central bulge and disk. [Minniti et al. \(2018\)](#) studied a more massive GC (M62) using its extra-tidal RRL population, discussing that modeling of tidal disruption and cluster mass loss is vital when the cluster is at its pericenter. Mass loss from bulge GCs could be considerable, changing the progenitor mass and the orbit over time. Dynamical friction and tidal evaporation must be included for better treatment of the past and future behavior of these systems.

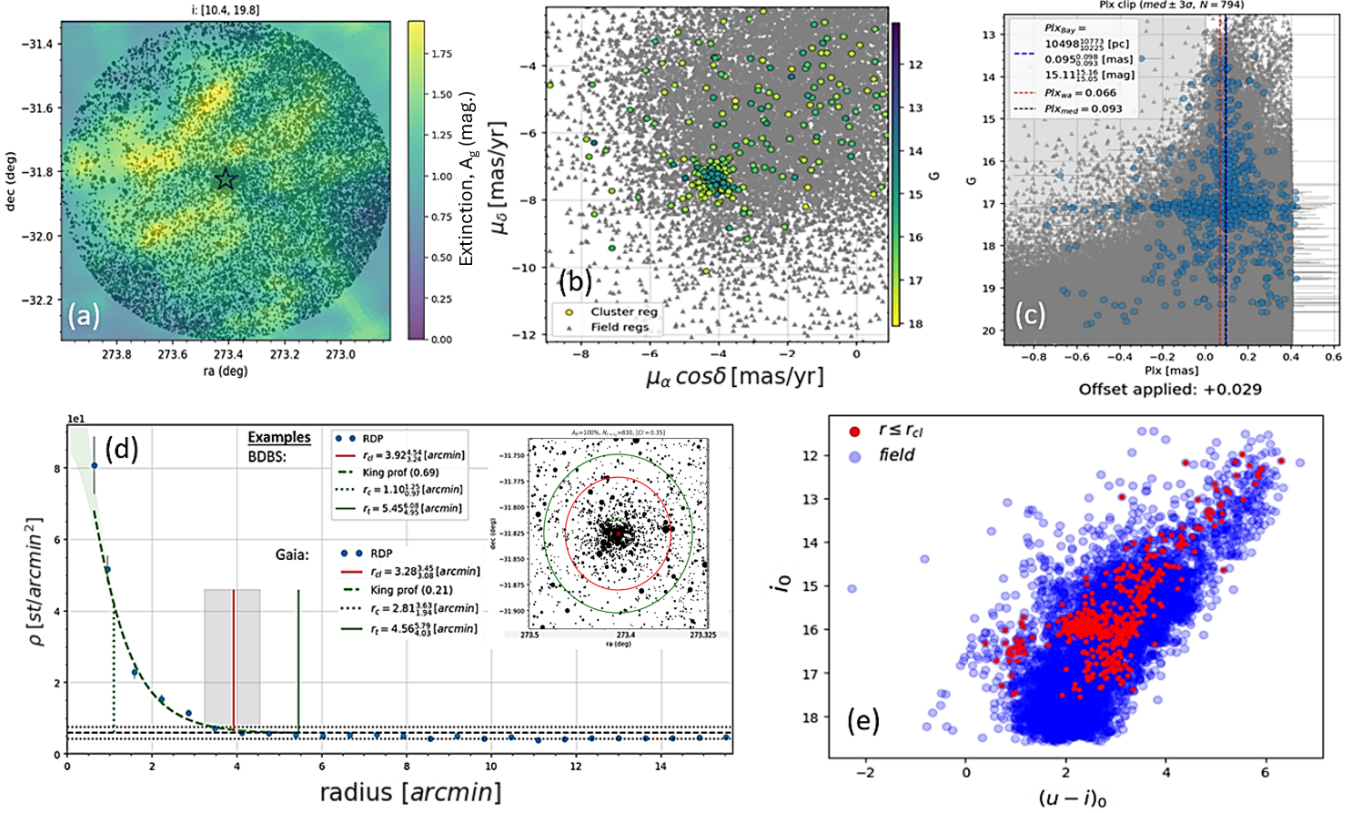


Figure 1. These diagrams are produced by the AStECA code (Perren et al. 2015). (a) The RA($^{\circ}$) vs. Dec($^{\circ}$) plot for 18,180 objects, with the black dots sized by the BDBS i-band magnitudes between 10.4 and 19.8 (with cataloged Gaia DR3 proper motions), in the NGC 6569 field. All the objects shown are within 30' of the cluster center. The extinction map in the BDBS g-band is overlaid (Kader et al. 2023), with the cluster center identified as a black open star. (b) The proper motions in R.A. (α) and Declination (δ) are plotted (in mas/yr), with the objects within 4' of the center of NGC 6569 shown as shaded circles, color-coded by their Gaia G-band magnitudes. The rest of the objects are shown as gray triangles. (c) The Gaia parallaxes of the objects marked as sharing the proper motion of the GC in part (b) are displayed as blue circles, and the rest are great triangles. We use objects with Plx values less than 0.4 mas/yr to exclude foreground stars. AStECA calculated the distance to NGC 6569, using Bayesian statistics (Perren et al. 2015) where $D = 10.498^{+0.275}_{-0.273}$ kpc. (d) We show an example of the King model (King 1962, 1966) fits to the BDBS photometry file, with the results for both the BDBS data and the independently-searched Gaia DR3 region as examples. The AStECA fits for the best-fit King model are given. (e) Using the reddening map (extended to all bands) from part (a), we show i vs. $(u-i)$ as a BDBS dereddened CMD for all the stars with our parallax limits. Faint, blue-shaded circles denote those stars outside the cluster radius from the BDBS sample (red circle in Fig.1d), and those within the cluster radius are shaded red.

This dissolution would be consistent with theoretical models which suggest that bulge GCs within 2 kpc of the Galactic Center may have lost up to 80% of their initial mass to the surrounding field (Baumgardt & Hilker 2018). The double red clump (RC) of the bulge may be partly attributable to globular clusters losing stars to the general bulge population (Lim et al. 2021). In the halo, Piatti & Carballo-Bello (2020b) found “53 globular clusters included in the final compilation, 14 have observed tidal tails, 22 have extra-tidal features that are different from tidal tails, and 17 present undetectable signatures of extra-tidal structures.” Unlike halo globular clusters, such as Pal 5 (Odenkirchen et al. 2001, 2003; Grillmair & Dionatos 2006; Erkal et al. 2017), detecting tidal debris around bulge GCs has proven challenging. Only a few bulge GCs, such as NGC 6355 & NGC 6362, exhibit detectable tidal features (Zhang et al. 2022; Piatti 2024a,b). Whether tidal debris from such processes can be detected in the dense and dusty bulge remains uncertain.

Mauro et al. (2012) included NGC 6440 in their study, highlighting the discovery of two distinct clumps along the horizontal branch (HB) of NGC 6569, detected using infrared photometry from the VISTA Variables in the Vía Láctea (VVV) Survey Minniti et al. (2010). NGC 6569 hosts two red HBs separated by about 0.1 mag in the K_S -band. J18 analyzed new and archival high-resolution spectra ($R \sim 27,000$) from Magellan–M2FS and VLT–FLAMES to determine the radial velocities and chemical compositions of red giant branch (RGB) and HB stars in and around NGC 6569. Both HB populations were found to move with the cluster, but the brighter HB stars were only 0.13 dex more metal-rich than the fainter population, a difference that was not statistically significant due to the small sample size (5 stars in each HB group). These findings were corroborated by analyses revealing the presence of blue HB stars, which are unusual in metal-rich clusters like NGC 6569 (Saracino et al. 2019). Dereddening the BDBS photometry makes structures in the HB visible in Fig.1e and Fig.2a, using the i_0 vs. $(u - i)_0$ and g_0 vs. $(u - g)_0$ color-magnitude diagrams (CMDs), respectively.

137 Clusters such as Terzan 5 and Liller 1 are considered to be remnants of larger systems containing
 138 both ancient (~ 12 Gyr) and younger (1-3 Gyr) populations (Ferraro et al. 2009, 2016; Ferraro et al.
 139 2021, and references therein). GCs with extended blue and red HBs, such as NGC 6441 and NGC
 140 6388, are unusual and part of the bulge population. For NGC 6569, J18 could not rule out helium
 141 abundance variations ($Y \sim 0.02$ dex) as a potential explanation for its abnormal HB (see Fig. 1e
 142 and Fig. 2a). J18 determined a mean RV of $-48.8 \pm 5.3 \text{ km s}^{-1}$ for the cluster and emphasized the
 143 need for metallicity measurements to distinguish cluster members from the surrounding bulge stars
 144 (illustrated in Fig. 1b). J18's data also yielded a mean $[\text{Fe}/\text{H}] = -0.87 \pm 0.05$ dex based on 19 M2FS
 145 spectra and $[\text{Fe}/\text{H}]_{CaT} = -0.84 \pm 0.17$ dex from 100 FLAMES spectra (hereafter, $[\text{Fe}/\text{H}]_{J18}$). The
 146 latter dataset is used as a comparison in this paper.

147 P23's recent kinematic study combined data from the ESO-VLT Multi-Instrument Kinematic Survey
 148 of Galactic GCs with four different instruments. Their sample spanned stars from $0.8 - 770''$ from
 149 the cluster center-outside the tidal radii of all studies reported in Table 1. By combining velocity
 150 data, PMs from Gaia DR3, and star counts to fit King models, P23 identified a “hint of ordered
 151 rotation” at $40'' < r < 90''$ from the cluster center, though they cautioned that more data are needed
 152 to confirm this.

153 2. OBSERVATIONS AND DATA REDUCTION

154 2.1. Target selection

155 This project uses the Blanco DECam Bulge Survey (BDBS) catalog (Rich et al. 2020; Johnson
 156 et al. 2020) and the Gaia DR3 data to select targets for the spectroscopic survey, using the u - and
 157 i -bands, shown Fig. 2b. This field-of-view (FOV) is extremely crowded: selecting the target sample
 158 using the PM of the cluster (matched with Gaia DR3) with $-3.13 > \mu_\alpha \cos(\delta) > -5.12$ mas/yr and
 159 $-5.85 > \mu_\delta > -8.85$ mas/yr, yielded 18,180 sources with $i > 19$ mag. Using the CMDs combined
 160 with the J18 and P23 spectroscopic surveys, we set the search parameters to identify NGC 6569's
 161 escaped stars. Within the cluster radius (the red circle in Fig. 1d), we selected $\sim 600 - 700$ members
 162 by using ASteCA (red-filled circles in Fig. 1e). For the initial project, we isolated potential extra-tidal

stars from the BDDBS i_0 vs. $(u - i)_0$ color-magnitude diagram with color and magnitude constraints from α -enhanced MIST isochrones (Choi et al. 2016). The initial comparison stars were within $1.2'$ of the cluster center, applying constraints on parallax ($Plx \leq 0.4$ mas) and proper motion to exclude obvious foreground objects (Fig.1c and Fig.2b), maximizing the chances of selecting an escapee from NGC 6569 from the surrounding sea of bulge stars. Comparing our data with the published surveys of J18 and P23, using radial velocities and metallicities allows us to associate extra-tidal stars with the GC population within the tidal radius of $\sim 6.9'$ (Harris 2010; Valenti et al. 2011), which was revised upwards to $9.98'$ by P23.

2.2. Spectroscopic Observations

As detailed in Kunder et al. (2024), we used the AAOmega multifibre spectrograph at the 3.9-m Anglo-Australian Telescope (Siding Spring Observatory, Coonabarabran, NSW, Australia). The spectra taken around NGC 6569 were part of a five-night observing run between July 20th and July 24th, 2022 (PROP-ID: O/2022A/3002). The plate configurations for the Two Degree Field (2dF) fibre positioner contained a combination of RRL stars (including four in the center of the cluster), RC stars, HB stars, and giants centered on the cluster (Fig.2), half-filling the 2-degree field of view, as shown in Fig.2b, at the lower right. This run also produced data on BH 261 (Kunder et al. 2024) and Patchick 99 (Butler et al. 2024), also shown as heavy black circles.

We employed the red 1700D grating (centered at 8600 Å) to detect the CaT lines for all objects and the blue 2500V grating (centered at 5000 Å) to detect the Mg line at 5180 Å in for the brightest stars. However, this paper only reports the results derived from the red spectra. Depending on weather and other factors, the exposure times ranged from 4×30 minutes to 2×30 minutes. Fig.3 shows examples of the spectra with the full range in signal-to-noise (S/N): these example stars with approximately the radial velocity (RV) NGC 6569.

The AAO 2dfdr pipeline (AAO Software Team 2015) was used to reduce the spectra: bias subtraction, cosmic ray cleaning, quartz flat-fielding, wavelength calibration via arc-lamp exposures, and sky subtraction using dedicated sky fibers. The spectra analyzed in this paper have a wavelength range of 8420-8800 Å, with slight variations depending on the exact position of the spectra on the CCD.

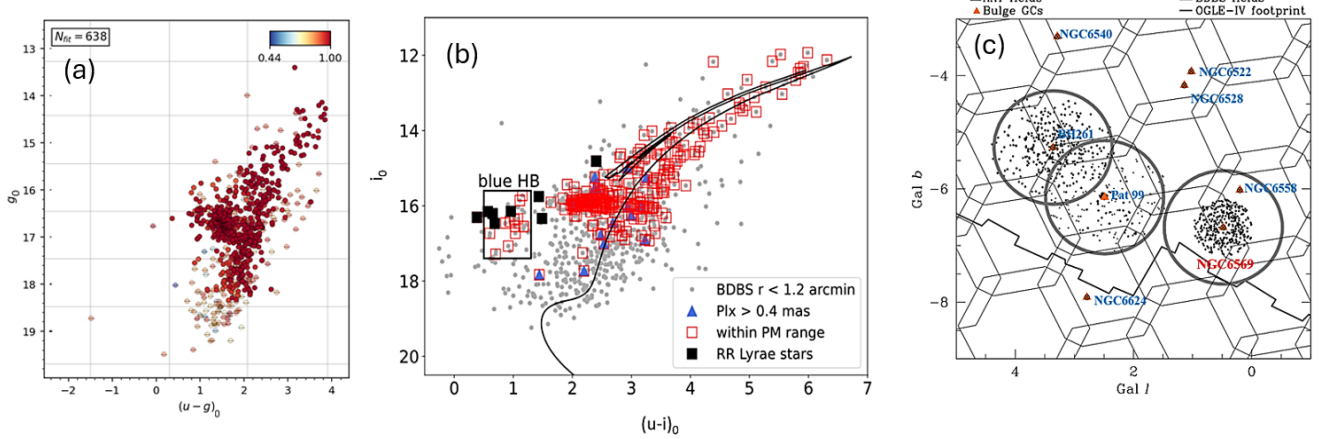


Figure 2. (a) The BDBS dereddened CMD for g vs. $(u-g)$ is displayed, corrected by the BDBS reddening maps (Kader et al. 2023), with the AStECA membership probabilities for 638 objects within the cluster radius. (b) The BDBS dereddened CMD for i vs. $(u-i)$ is shown. The small, gray filled circles are the stars within $1.2'$ of the center of NGC 6569. The following objects are identified within 5 tidal radii of the center of the cluster: stars within 0.95° of the cluster center; stars must have a proper motion within 1 mas/yr in R.A. and within 1.5 mas/yr in Dec of the main cluster proper motion: ($\sim -4.125 \pm 1.0$ mas/yr, $\sim -7.354 \pm 1.5$ mas/yr). Additional constraints were applied: objects with BDBS u -magnitudes with uncertainties < 0.04 mag. were selected if they had detections in the BDBS g - and i -bands also. The red open squares were identified as targets for AAT/AAOmega spectroscopy. Blue triangles are flagged as likely foreground objects, and black-filled squares are identified as RRLs. The isochrone shown is from the MIST models (Choi et al. 2016), $[Fe/H] = -0.75$ dex, $[\alpha/Fe] = +0.3$ dex, with an age of 13 Gyr. (c) The large gray circles are our AAT test fields. Circles with crosses identify globular clusters from the Baumgardt et al. (2021) catalog of galactic globular clusters, with the orange triangles indicating the bulge globular clusters. The footprints of the BDBS and OGLE surveys are indicated by thin and bold black lines, respectively.

190

2.3. Radial velocities and $[Fe/H]$ measurements

191 The CaT lines are among the strongest features in the near-infrared spectra of late-type stars,
 192 making them relatively easy to detect even in faint objects (Grocholski 2006; Carrera et al. 2007).
 193 This strength is advantageous when observing distant or low-luminosity stars, as it allows for accurate
 194 measurements of equivalent widths, which are crucial for deriving metallicities. The prominence of
 195 these lines enables us to obtain reliable data from stars that might otherwise be too faint for detailed

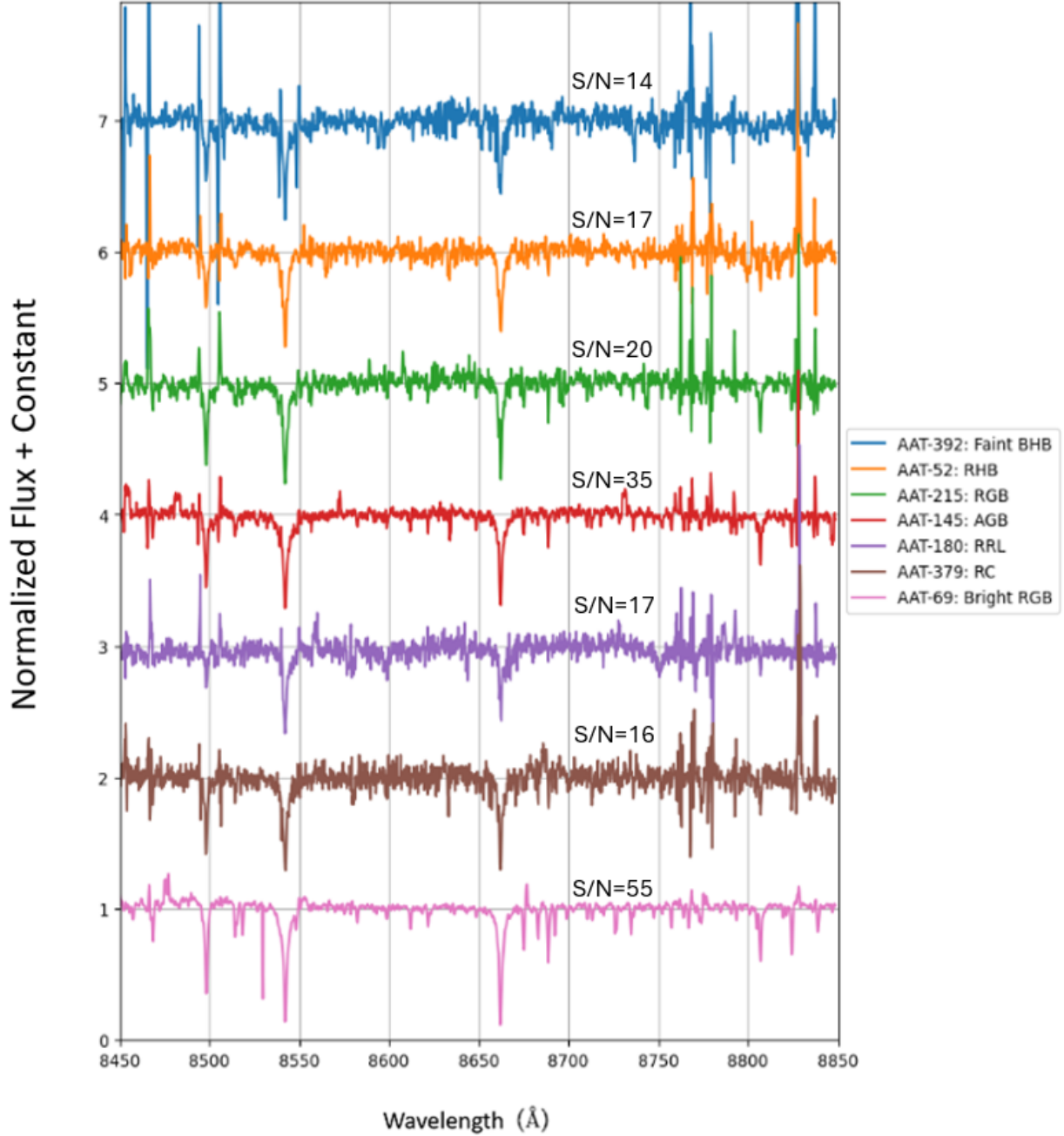


Figure 3. Examples of the AAT/AAOmega spectra analyzed in this work, labeled with their approximate locations on the CMD and the average spectral S/N, calculated from the CaT measurements and the SP_Ace code. The AAT fiber numbers correspond to objects listed in Table 2, identified by their position on the CMD shown in Fig.2b.

analysis using optical lines, which are often weaker and more susceptible to blending with other spectral features (Cole et al. 2004).

As with the BH 261 spectra (Kunder et al. 2024), RVs were measured with IRAF's `xcsao` routine (Kurtz et al. 1992). This process cross-correlates against spectra from three stars observed during the same run and used as templates, chosen from the Apache Point Observatory Galaxy Evolution Experiment (APOGEE, Eisenstein et al. 2011) database. Kunder et al. (2024) used APOGEE 2M18134674-2926056 (RV=27.88±0.03), APOGEE 2M17514997-2906055 (RV=−187.33±0.02) and APOGEE 2M17521244-2919510(RV=65.13±0.05) as RV-templates, yielding a median velocity error of ~ 3 km s $^{-1}$ for the upper RGB and 9 km s $^{-1}$ for the fainter and hotter HB stars. The barycentric correction was made using the PyAstronomy routine, to match the APOGEE results to the catalog standard frame of reference.

Fig.4a illustrates an example spectrum of one red giant branch (RGB) object (#215 in Table 2), showing the CaT method of determining the RV from an average of the shifts of the 3 CaT lines, and measuring their equivalent widths, after normalizing the spectrum (Fig.4a). In Fig.4b, the normalized stellar spectrum is shown in gray, with the SP_Ace model-fits (Boeche & Grebel 2016; Boeche et al. 2021, § see 2.3.2) shown using the CaT lines (blue), and using the CaT lines in the fit (green). The results for the best fits are given in Tables 3 and 4.

213 2.3.1. *CaT Calibration*

For the calibration of CaT equivalent widths (EWs) to [Fe/H], we used the Dias & Parisi (2020) calibration using the i-band, and compared that to the K-band calibration used by J18 for 98/100 stars reported in that paper, identified with BDDBS photometry. We used:

$$217 \sum EW = EW_{8498} + EW_{8542} + EW_{8662} \quad (2)$$

and

$$219 \sum EW = W'_m - \beta_m(m - m_{HB}) \quad (3)$$

for the DECam i-band filter. $\beta_i = 0.62 \pm 0.06 \pm 0.17$, where the first error is the formal uncertainty and the second is the standard deviation. The luminosity correction is taken to be the position of the

222 HB in the i-band, which is $i = 16.587$ mag. (with reddening). We found that including the reddening
 223 correction changed the final [Fe/H]-value by $< \pm 0.05$ dex.

224 J18 and most other studies only used the redder 2 CaT lines; we calculated values, using:

$$225 \quad \sum EW_{3L} = 1.26(\pm 0.13) + 1.00(\pm 0.03) \cdot EW_{2L} \quad (4)$$

226 and obtaining

$$227 \quad \sum [Fe/H]_{DP} = 2.966(\pm 0.032) + 0.362(\pm 0.014) \cdot W' \quad (5)$$

228 We report all the EWs and RVs for the sample of 303 spectra in Table 2, but only complete the
 229 calculation for the 58 stars within the expected range of $-25 > RV > -65 \text{ } km s^{-1}$, where it is
 230 expected that *some* of the extra-tidal stars will be at the same distance as NGC 6569. This range is
 231 $-30 > RV > -63 \text{ } km s^{-1}$ from J18, but the AAOmega spectra have a greater average uncertainty of
 232 $\sim 3 \text{ } km s^{-1}$ than the J18 sample. The RVs and EWs for the CaT lines were measured for the entire
 233 AAT-sample.

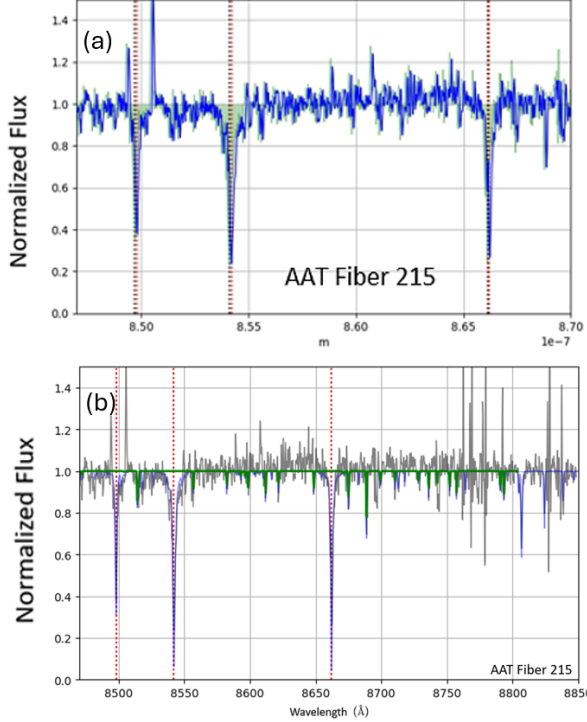


Figure 4. An example of the spectral analysis process for one star is shown in these two panels using an extracted, processed spectrum for AAT/AAOmega fiber No. 215 (units: Jy vs. m). (a) The normalized spectrum is shown in blue, with the fill to the continuum indicated by green shading. Fiber No. 215 has $RV = -49.7 \pm 2.1 \text{ km s}^{-1}$ sharing the PM and RV of NGC 6569 and $S/N = 20$. The centroid of each CaT feature is shown as a black dotted line, with the rest wavelength indicated as a gray dotted line in all cases. We used the ‘specutils’ routine to find lines by the derivative method and averaged the results for the three CaT lines. (b) In this panel, the normalized spectrum is shown in gray. The spectrum has been shifted to the lab frame, with the centroids of the CaT lines indicated by red dotted lines. The SP_Ace code ([Boeche & Grebel 2016; Boeche et al. 2021](#)) fit for the whole region is shown in blue, and another SP_Ace model-fit avoiding the CaT lines is shown in green. The results for this star are: $[Fe/H]_{DP} = -0.92 \pm 0.09$ dex, $[Fe/H]_{SP} = -0.83 \pm 0.08$ dex, and $[\alpha/Fe] = +0.27 \pm 0.27$ dex.

Table 2. DBBS Data & Extinction Corrections

No.	ID	RA($^{\circ}$)	Dec($^{\circ}$)	u	σ_u	g	σ_g	r	σ_r	i	σ_i	z	σ_z	y	σ_y	A_u	A_g	A_r	A_i	A_z	A_y
1	572800	273.95715	-31.84990	20.046	0.014	17.557	0.004	16.508	0.009	15.937	0.004	15.616	0.003	15.413	0.007	1.562	1.247	0.915	0.677	0.521	0.415
2	555243	273.80745	-31.83143	20.000	0.039	17.048	0.001	15.879	0.008	15.269	0.002	14.917	0.011	14.675	0.011	1.707	1.363	1.000	0.740	0.570	0.454
3	576699	273.99068	-31.82702	19.640	0.021	16.908	0.004	15.841	0.008	15.290	0.001	14.962	0.007	14.757	0.011	1.348	1.076	0.790	0.585	0.450	0.358
4	567026	273.92156	-31.82735	20.300	0.018	17.812	0.001	16.703	0.007	16.097	0.003	15.736	0.007	15.537	0.002	1.681	1.342	0.985	0.729	0.561	0.446
5	575629	273.97991	-31.86273	19.801	0.034	17.424	0.012	16.384	0.009	15.814	0.001	15.456	0.004	15.270	0.014	1.418	1.132	0.831	0.615	0.473	0.377

Note—The complete table is available online.
DBBS DECam filters and extinction corrections by Simion et al. (2017)

Table 3. Gaia Data & CaT Measurements

No.	RA	Dec	Plx	σ_{Plx}	$\mu_{\alpha} \cos(\delta)$	$\sigma_{\mu_{\alpha}}$	μ_{δ}	$\sigma_{\mu_{\delta}}$	RV	σ_{RV}	S/N	EW_{8498}	EW_{8542}	EW_{8662}	$[Fe/H]_{DP}$	$\sigma_{[Fe/H]_{DP}}$
1	273.957165	-31.84991691	0.0276	0.0740	-3.2532	0.0714	-5.9616	0.0564	91.829	1.338	16	1.287	3.39	1.835	-0.76	0.01
2	273.8074592	-31.83144141	0.1228	0.0457	-3.2069	0.0491	-8.3173	0.0369	35.548	2.212	16	1.586	4.174	2.497	-0.33	0.08
3	273.9906913	-31.82703443	-0.0024	0.0617	-4.3467	0.0529	-8.2425	0.0403	137.431	3.022	31	1.094	3.225	2.361	-0.81	0.04
4	273.9215763	-31.82736076	0.1325	0.0820	-4.7706	0.0742	-6.5152	0.0555	40.882	1.683	26	1.077	3.180	1.520	-0.95	0.05
5	273.9799231	-31.86274321	0.1656	0.0687	-3.2174	0.0617	-8.1999	0.0449	40.882	1.683	21	1.002	3.277	2.126	-0.77	0.07
6	273.7112686	-31.9520028	0.0938	0.0589	-3.5443	0.0759	-8.3998	0.0577	142.775	1.043	20	0.822	3.300	1.865	-0.82	0.11
8	273.8535969	-31.85689585	0.1267	0.0614	-4.8357	0.0571	-7.0317	0.0440	-49.667	2.124	25	1.172	3.123	2.345	-0.75	0.02
9	273.7537892	-31.84696467	0.1871	0.0488	-3.8984	0.0629	-7.0789	0.0471	-61.011	2.434	31	1.077	3.071	1.894	-0.94	0.05
12	273.7545289	-31.83672078	0.0102	0.0578	-4.5130	0.0685	-8.0424	0.0517	29.552	3.996	31	1.208	2.735	1.872	-1.00	0.01
13	273.6978755	-31.867033	0.1321	0.0779	-4.0546	0.0927	-7.4150	0.0704	145.614	4.712	20	0.945	3.147	2.269	-0.58	0.08
14	273.7487791	-31.90074517	0.0614	0.0798	-4.2935	0.1015	-6.4192	0.0790	114.503	3.497	23	1.165	3.016	2.260	-0.63	0.02

Note.—The complete table is available online.

Assuming that all stars are at the same distance of 10.53 kpc.

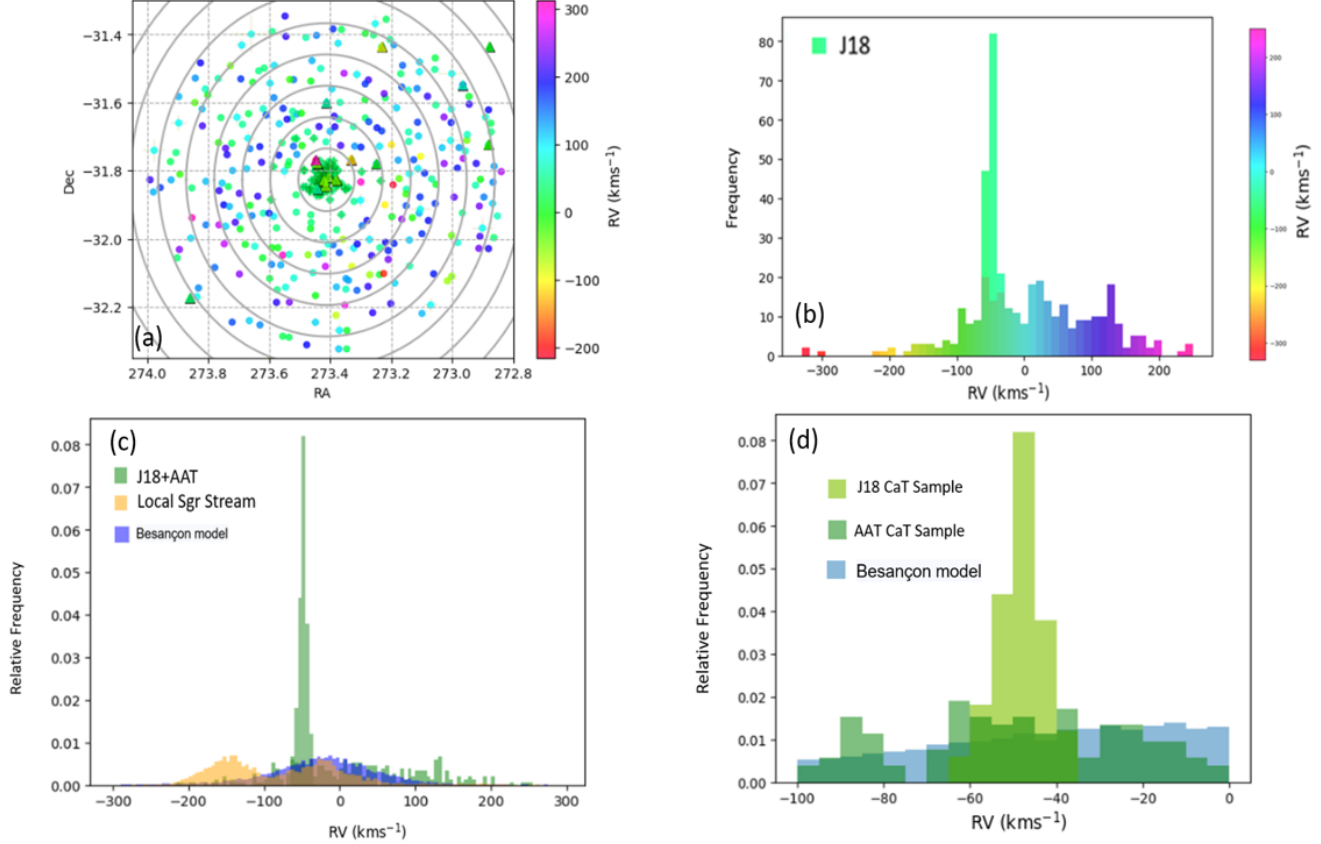


Figure 5. (a) A plot of the RA vs. Dec positions of the 303 spectroscopic targets (2 fibers did not yield measurable spectra) in and around NGC 6569 (shaded circles), along with some known RR Lyrae stars (from OGLE) with catalogued RVs (filled triangles). The circles are color-coded by RV (see color bar on the right). The 100 objects from J18 are shown as green crosses in the cluster center. The gray circles are successive tidal radii (Ortolani et al. 2001; Valenti et al. 2011, 6.9') from the center of NGC 6569. P23 found a greater value of 589.7''. (b) The absolute number of stars per bin is shown in this histogram of the total RV-range, shaded with the color bar on the plot's right side. The 100 stars in the J18 sample with RVs and CaT-metallicities are shown in green behind the AAT sample. (c) The combined J18 and AAT data are shown in this relative frequency histogram in transparent forest green, the local Sgr Stream is shown in gold (Ramos et al. 2022), and the Besançon models (Robin 2012) for our FOV is shown in violet. (d) The zoomed-in relative frequency histogram of the NGC 6569 cluster region is shown with the J18 data in olive green, the AAT data in forest green, and the Besançon model in blue for our FOV and PM ranges.

The RV-map is shown in Fig.5a, with the color-coded circles being all the 303 AAT AAOmega spectra, the triangles are the local RRLs, and the green crosses are the J18 sample. Each successive

gray circle is a 1-5 tidal radii. Fig.5b superimposes the J18 (bright green) sample on our data, in absolute numbers. In Fig.5c, comparisons are made between the source density histograms for NGC 6569's FOV and the local Besançon (Czekaj et al. 2014) model population, using the PM limits, also comparing with the local Sgr Stream stars (Ramos et al. 2022). Fig.5d zooms in on the J18-defined range of RV for NGC 6569, with the AAT sample and the Besançon models, shown as relative frequency histograms. The Besançon models are consistent with the bulge field stars contaminating the cluster by about 35%, as indicated by Equation (1).

2.3.2. Abundance Analysis

SP_Ace (Stellar Parameters and Chemical Abundances Estimator), is an open-source tool for deriving stellar parameters and elemental abundances from stellar spectra. Recent updates support $R = 2000 - 40,000$, where the AAT spectra have $R \sim 11,000$. SP_Ace utilizes the General-Curve-of-Growth (GCOG) library which is based on 6700 absorption lines with astrophysically-calibrated oscillator strengths. Following on from the work of Kunder et al. (2024) at al. (2024) in BH 261, we used the SP_Ace code (Boeche & Grebel 2016; Boeche et al. 2021) to determine the [Fe/H] metallicities for the brighter giants. The S/N of individual spectra ranged from 14 to 55 (Fig.3). The CaT lines for all 303 spectra were measured; only spectra with $S/N > 35$ or $[\alpha/Fe]_{SP} > +0.20$ dex were suitable for robust chemical abundance analysis beyond the iron lines, as we found that poorer quality spectra would only yield lower limits on the $[\alpha/Fe]_{SP}$ abundances.

SP_Ace compares spectra to models over the wavelength intervals, 4800-6860 Å 8400-8924 Å. The tool was designed for the Radial Velocity Experiment (RAVE) (Kunder et al. 2017; Steinmetz et al. 2020). Under ideal conditions, SP_Ace can measure individual abundances for different chemical species (Mg, Al, Si, Ca, Ti, Fe, and Ni), but only [Fe/H] abundances are reliable for the whole AAT data set. Under $S/N \sim 35$, spectra give the most reliable results for the Fe I and Fe II lines (Fig.4b). The spectra were fit over different wavelength ranges and the best results were obtained by avoiding the strong CaT lines.

The ‘alpha’ mode instructs SP_Ace to assume the spectrum as if there were only two elements: ‘metal’ and ‘alpha’ (not counting C, N, O or CN as α -elements), where ‘alpha’ mode should improve

model fits to spectra with lower resolution than the $R \approx 11,000$ in our AAT sample. The red dotted lines show the case where there was an exact correspondence between the measurements. We find that for spectra with $S/N > 35$ (Fig.6):

(a) $[Fe/H]_{SP} = 1.000(\pm 0.000)[m/H]_{SP} + 0.0349(\pm 0.0130)$ and $R^2 = 1.000$, for 79 objects over the range: $+0.5 > [Fe/H]_{SP} > -1.30$ dex.

(b) For the same 79 objects:

$[\alpha/Fe]_{SP} = 0.955(\pm 0.028)$, $[\alpha/m]_{SP} - 0.0231(\pm 1.479)$ with $R^2 = 0.938$ over the range $+0.6 > [\alpha/m]_{SP} > -0.1$ dex.

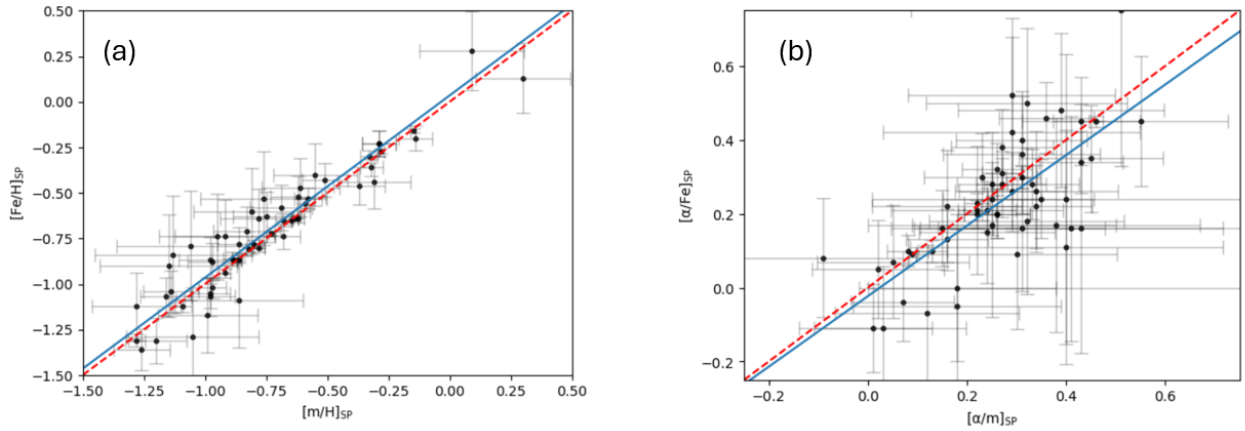


Figure 6. Using spectra with $S/N > 35$ for 79 objects: (a) The plot of $[Fe/H]_{SP}$ vs. $[m/H]_{SP}$, where the red dotted line is where $[Fe/H]_{SP} = [m/H]_{SP}$ and the blue line is the fit $[Fe/H]_{SP} = 1.000(\pm 0.000)[m/H]_{SP} + 0.0349(\pm 0.0130)$ and $R^2 = 1.000$, over the range: $+0.5 > [Fe/H]_{SP} > -1.30$ dex (b) $[\alpha/Fe]_{SP}$ vs $[\alpha/m]_{SP}$ where the red dotted line is $[\alpha/Fe]_{SP} = [\alpha/m]_{SP}$. The blue line is the fit of $[\alpha/Fe]_{SP} = 0.955(\pm 0.028)$, $[\alpha/m]_{SP} - 0.0231(\pm 1.479)$ with $R^2 = 0.938$ over the range $+0.6 > [\alpha/m]_{SP} > -0.1$ dex.

Of 72 of the public ESO spectra we could extract and match with the BDBS photometry used by P23, only 10 were not badly contaminated by night-sky lines around the $CaT3 = 8662\text{\AA}$ absorption feature. Thus, the CaT-calibration method was not used for this sample. The ESO spectra were run through SP_Ace and the results are shown in gold in Fig.7a. The J18 sample contains 100 stars; we

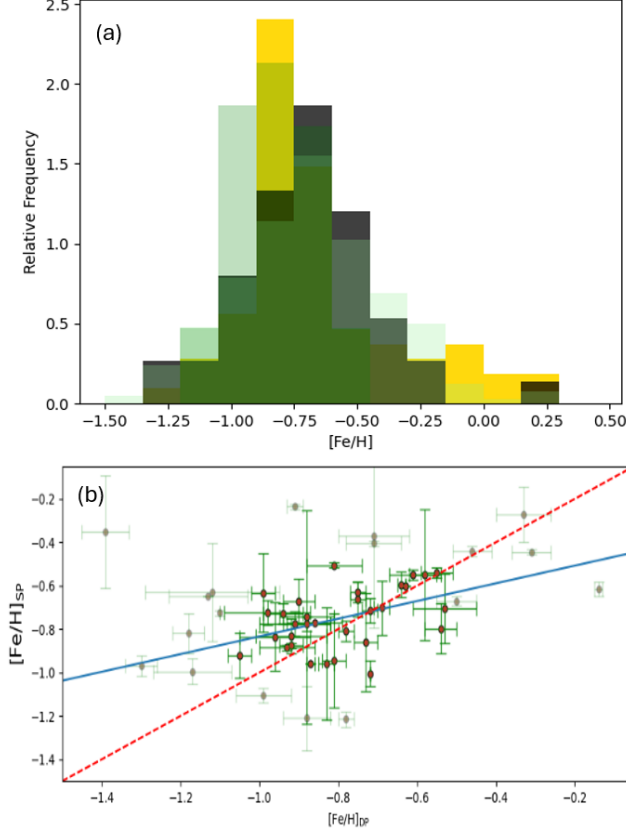


Figure 7. Comparisons between the calibration methods of obtaining $[Fe/H]$ from the CaT lines (Dias & Parisi 2020, J18) with the SP_Ace code results. (a) A comparison of the relative frequency histograms of the various samples of stars compared in this paper: all 72 stars from the extracted ESO archive are shown in gold (SP_Ace), all 281/303 stars from the AAT sample are shown in black (SP_Ace), 100 stars from J18 are shown in green ($[Fe/H]_{J18}$ CaT), and the 58 stars with $-65 < RV < -25 \text{ km s}^{-1}$ are shown in light green ($[Fe/H]_{DP}$). (b) The direct comparison between $[Fe/H]_{DP}$ and $[Fe/H]_{SP}$ for the 58 stars (all shown as faint gray circles with error bars) with $-65 < RV < -25 \text{ km s}^{-1}$ exhibits a weak trend between $-0.5 > [Fe/H]_{SP} > -1.1$: $[Fe/H]_{SP} = 0.408(\pm 0.157)$ $[Fe/H]_{DP} - 0.426(\pm 0.127)$ with $R^2 = 0.188$ (blue solid line). Some of the 58 extra-tidal candidates may be at a different distance in the bulge than NGC 6569-meaning that the $(i - i_{HB})$ luminosity correction will not be accurate. For individual stars, the CaT calibration should measure $[Fe/H]$ within ± 0.3 dex (J18), shown by the red dotted line.

took their data from the source paper, reconciled the calibration between the i - and K_S -bands (Dias et al. 2022), and show the J18 sample in green. Of the AAT 303 stars, 281 objects had reported $[Fe/H]_{SP}$ values (black), but only 58 stars fit the criteria to be in the velocity range of NGC 6569,

allowing for $[Fe/H]_{DP}$ to be valid, which we show in light green. Even before making any metallicity cuts, Kolmogorov–Smirnov (K-S) tests between the [Fe/H]-samples indicated they were all drawn from the same underlying population.

Comparing the results of $[Fe/H]_{SP}$ and $[Fe/H]_{DP}$ for the RV restricted sample in Fig.7b, some of the 58 extra-tidal candidates may be at a different distance in the bulge than NGC 6569, where the $(i - i_{HB})$ luminosity correction will not be accurate. J18 discussed that for individual stars, the CaT calibration should measure [Fe/H] within ± 0.3 dex. We find that $[Fe/H]_{DP}$ returns $[Fe/H]_{SP}$ to within ± 0.3 dex for individual stars having $-0.5 > [Fe/H]_{DP} > -1.1$ dex (heavier green circles filled with orange: fit shown with the red dotted line). We tabulate the absolute value of the difference between the methods of estimating [Fe/H] as $\Delta[Fe/H] = |[Fe/H]_{SP} - [Fe/H]_{DP}|$ in Table 4.

2.3.3. Extra-Tidal Candidates

Of the 303 measurable spectra, 58 ($19 \pm 4\%$) fell in the allowed RV range of $-25 > RV > -65 \text{ km s}^{-1}$ and are the initial extra-tidal candidates. Of those, 40 stars fell in the $-0.5 > [Fe/H] > -1.1$ dex limit for $[Fe/H]_{SP}$ and 50 stars were in that range for the CaT-method ($[Fe/H]_{DP}$). Fig.8 shows the results of the SP_Ace modeling for the 281 objects inside the temperature range 7500–3500K that we were able to fit with the code on a Tinsley–Wallerstein diagram (Wallerstein, G. 1962; Tinsley 1979). Koch et al. (2019) used SP_Ace for Pal 15, and found typical T_{eff} uncertainties of $\sim 80\text{K}$, with $\log g$ uncertainties of ~ 0.25 dex. The 303 stars in the AAT sample are shown as small RV-color-coded circles with light gray error bars. The 10 best ESO spectra are shown as gold-filled squares with black borders. The PM-selected Besançon models for our PM-selected FOV are shown as small black dots. Again, SP_Ace was only able to give lower limits on $[\alpha/Fe]_{SP}$ for the low S/N spectra. Fig.8b shows the AAT data set with $S/N > 35$ and/or $[\alpha/Fe]_{SP} > +0.15$ dex. There are 67/303 objects with either sufficient S/N or α -enhancement typical of GCs. For all the AAT sample: 44/303 have $S/N > 35$, with 9 stars within $-25 > RV > -65 \text{ km s}^{-1}$.

Table 4. Extra-Tidal Candidates & Non-Members

Fiber No.	[M/H]	$\sigma_{[M/H]}$	$[Fe/H]_{SP}$	$\sigma_{[Fe/H]_{SP}}$	$[\alpha/Fe]_{SP}$	$\sigma_{[\alpha/Fe]_{SP}}$	T	σ_T	Log g	$\sigma_{Log g}$	RV	σ_{RV}	S/N	$[Fe/H]_{DP}$	$\sigma_{[Fe/H]_{DP}}$	$\Delta[Fe/H]_{DP}$	Class
Extra-Tidal Candidates																	
221	-0.70	0.08	-0.96	0.26	0.43	0.21	4258	50	1.91	0.76	-61.08	2.38	36.91	-0.83	0.02	0.13	A
84	-0.53	0.03	-0.87	0.01	0.45	0.01	4420	26	1.88	0.06	-61.01	2.43	36.56	-0.92	0.03	0.05	A
86	-0.32	0.14	-0.55	0.02	0.28	0.14	4865	37	2.64	0.33	-55.32	2.45	25.95	-0.61	0.06	0.06	A
321	-0.72	0.02	-0.96	0.00	0.34	0.01	4358	6	2.15	0.13	-44.03	2.31	31.28	-0.87	0.01	0.09	A
237	-0.67	0.08	-0.94	0.22	0.35	0.21	4576	72	2.85	0.75	-41.11	2.11	29.96	-0.81	0.03	0.13	A
325	-0.55	0.38	-0.77	0.03	0.37	0.41	5358	63	1.35	0.94	-41.11	2.11	19.92	-0.88	0.06	0.11	A
145	-0.62	0.09	-0.92	0.10	0.39	0.08	4928	99	2.76	0.18	-38.34	2.54	38.76	-1.05	0.03	0.13	A
292	-0.63	0.20	-0.86	0.23	0.26	0.18	4760	134	3.51	0.80	-63.85	2.40	28.65	-0.73	0.03	0.13	B
394	-0.63	0.05	-0.71	0.06	0.15	0.06	4722	19	2.98	0.09	-61.08	2.38	33.34	-0.72	0.02	0.01	B
9	-0.57	0.01	-0.73	0.05	0.23	0.08	4889	28	3.58	0.40	-61.01	2.43	33.15	-0.94	0.05	0.21	B
376	-0.46	0.01	-0.54	0.02	0.13	0.05	4364	11	2.67	0.05	-55.45	2.47	34.11	-0.55	0.04	0.01	B
31	-0.57	0.02	-0.81	0.05	0.34	0.06	4916	66	2.11	0.32	-55.32	2.45	31.34	-0.78	0.02	0.03	B
19	-0.74	0.09	-0.83	0.16	0.15	0.27	5047	7	2.41	0.14	-52.52	2.37	31.57	-0.96	0.09	0.13	B
215	-0.59	0.28	-0.83	0.08	0.27	0.28	4797	172	2.78	0.73	-49.67	2.12	20.43	-0.92	0.09	0.09	B
8	-0.51	0.02	-0.63	0.05	0.18	0.06	4540	42	3.04	0.06	-49.67	2.12	27.87	-0.75	0.02	0.12	B

Note.—The complete table is available online.

Class A(7): $-25 > RV > -65 \text{ km s}^{-1}, -0.5 > [Fe/H]_{SP} > -1.1 \text{ dex}$, and $[\alpha/\text{Fe}] > +0.2 \text{ dex}$.Class B(12): $-25 > RV > -65 \text{ km s}^{-1}, -0.5 > [\alpha/\text{Fe}] > -1.1 \text{ dex}$ and $[\alpha/\text{Fe}] > +0.1 \text{ dex}$.Class C(14): $-25 > RV > -65 \text{ km s}^{-1}, -0.5 > [\text{Fe}/\text{H}] > -1.1 \text{ dex}$ and $-0.1 < [\alpha/\text{Fe}] < +0.1 \text{ dex}$, or objects with only $[\text{Fe}/\text{H}]_{DP}$ in the correct range.Class D(8): $-25 > RV > -65 \text{ km s}^{-1}, -0.5 > [\text{Fe}/\text{H}] > -1.1 \text{ dex}$, but $\Delta[\text{Fe}/\text{H}] > 0.30 \text{ dex}$.Class RR(4): $-25 > RV > -65 \text{ km s}^{-1}$, and known RRL stars.

Class F(258): Stars either beyond the RV range for NGC 6569 or outside its metallicity range.

302 The 7,562 model stars contained in the Besançon sample for our FOV were selected using the same
 303 PM criteria as the spectroscopic target objects, with BDBS i-band magnitudes above the approximate
 304 brightness limit of 17.5 magnitudes (Fig.2b). Selecting for the heliocentric radial velocity (HRV)
 305 limits of $-25 \text{ to } -65 \text{ km s}^{-1}$, leaves 1660 objects (22%), but there are only 539 model stars with
 306 $-1.1 < [\text{Fe}/\text{H}] < 0.5$ dex, and $[\alpha/\text{Fe}]_{SP} > +0.2$ dex, which is 7%. We found 58/303 of our spectra
 307 in the same HRV range, which is 19%, and 41 stars were classed ABCD from Table 4, which is 14%.

308 Fig.8c shows the PM range expected for NGC 6569, with the AAT sample displayed as small filled
 309 circles, color-coded for RV. The 58 stars within $-25 > RV > -65 \text{ km s}^{-1}$ are shown as large black
 310 plus-signs, and the J18 sample is shown as small green crosses. We identify Djorg 1 and NGC 5139
 311 as the only GCs whose central PMs fall in this range. Fig.8d is a plot of $[\text{Fe}/\text{H}]_{SP}$ vs: RV: we show
 312 our 58 NGC 6569 extra-tidal candidates as black pluses, the J18 sample is again displayed as small
 313 green crosses. The objects outside the range of $-25 > RV > -65 \text{ km s}^{-1}$ are shown as small filled
 314 circles, color-coded by $[\alpha/\text{Fe}]_{SPSP}$, and stars with $S/N > 35$ are indicated by larger circles. The
 315 ‘local’ GC in the BDBS FOV are indicated as large stars, color-coded by $[\alpha/\text{Fe}]_{SP}$. NGC 5139 (ω
 316 Cen) is included because its unusual orbit takes it through the general area.

317 3. THEORETICAL MODELING AND COMPARISON WITH OBSERVATIONS

318 To accept or reject the 58 extra-tidal candidates, we compared their properties with theoretical
 319 models of tidal streams (Fardal et al. 2015) generated using the Gala Python package (Price-Whelan
 320 2017, 2022) designed specifically for galactic dynamics. It provides a user-controlled framework for
 321 simulating and analyzing the dynamics of stars and stellar systems within a chosen galactic potential.
 322 The code contains a collection of predefined potentials that represent different components of the
 323 Milky Way, such as the disk, bulge, and dark matter halo.

324 Gala also supports the transformation of orbital parameters into action space, which is a powerful
 325 method for the dynamical analysis of stellar populations (Vasiliev 2018). This feature is particularly
 326 relevant for studies involving tidal streams, such as those associated with GCs like Palomar 5, where
 327 the dynamics of the stream can provide insights into the gravitational potential of the Galaxy (Price-
 328 Whelan et al. 2019). Gala is built on top of `astropy`, a widely used library for astronomy-related

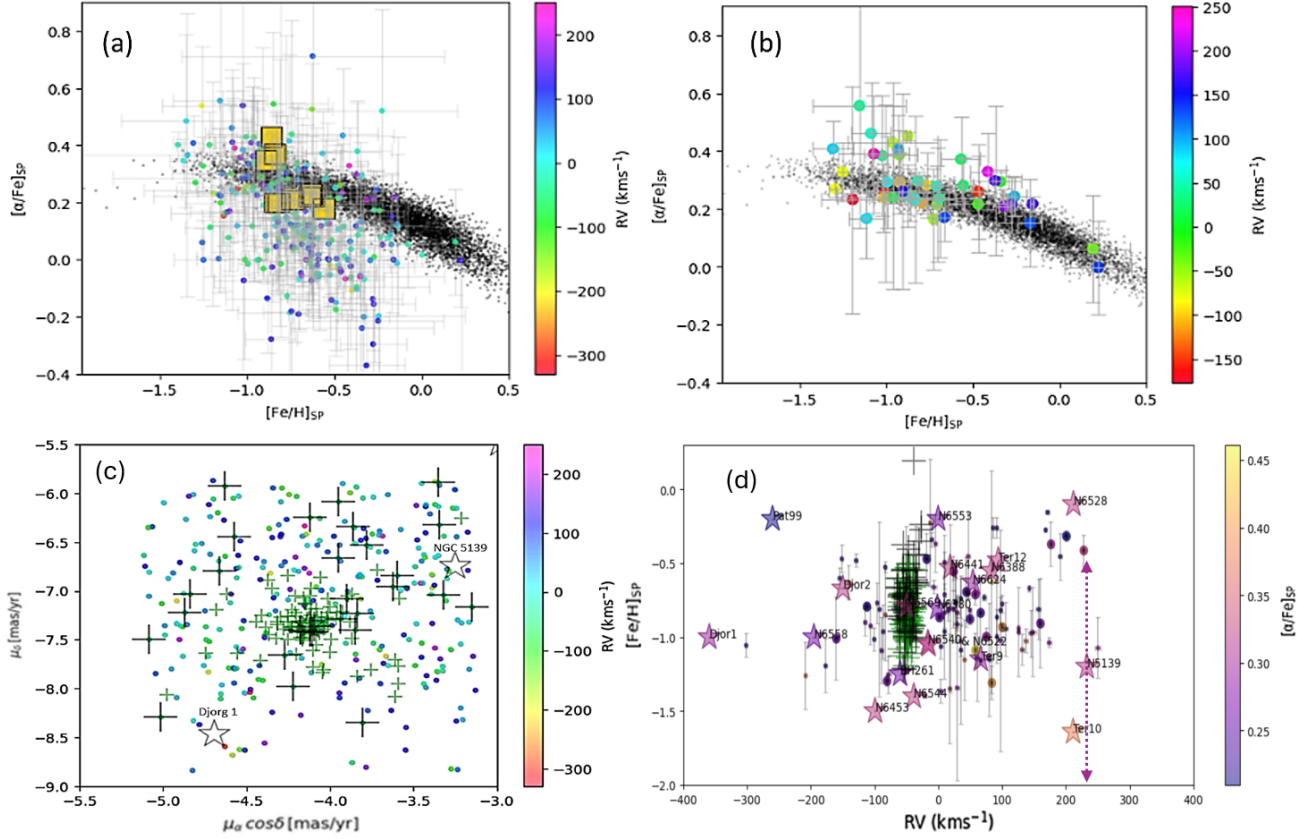


Figure 8. (a) The SP_Ace results for the whole sample: the $[\alpha/\text{Fe}]$ vs. $[\text{Fe}/\text{H}]$ plot. The Besançon Galactic models for our FOV are shown as gray dots. The 281 stars with spectra allowing the SP_Ace modeling are shown as small circles with error bars, color-coded by RV. The 10 spectra with minimal sky-line contamination selected from the ESO archives are the gold squares with black edges. (b) The 67/303 objects having spectra with $S/N > 35$, or $[\text{Fe}/\text{H}]_{\text{SP}} < -0.5$ and $[\alpha/\text{Fe}]_{\text{SP}} > +0.15$ dex, or $S/N > 35$ and any $[\alpha/\text{Fe}]_{\text{SP}}$ - or $[\text{Fe}/\text{H}]$ -value. Individual AAT/AAOmega spectra must have $S/N > 35$ or $[\alpha/\text{Fe}]_{\text{SP}} > +0.20$ dex for the α -abundances calculated by the SP_Ace code to be considered better than a lower limit. (c) A plot of the Gaia PMs for the spectroscopic sample of 303 stars (filled circles, color-coded by RV). Our extra-tidal sample of 58 RV-selected stars is shown as the black crosses. The small green crosses denote the J18 sample of 100 stars. Only the GC centers of Djorg 1 and NGC 5139 have PMs similar to that of NGC 6569. (d) The $[\text{Fe}/\text{H}]_{\text{SP}}$ vs. RV plot: the 58 NGC 6569 RV-matches are shown as gray crosses; the 100 stars of the J18 sample are shown as green crosses, non-RV-members of NGC 6569 are shown as small $[\alpha/\text{Fe}]_{\text{SP}}$ -color-coded circles, with those having $S/N > 35$ indicated as larger circles. The large stars are local bulge GCs or those with orbits passing near our FOV (not a comprehensive list).

computations in Python. This integration allows for compatibility with other astronomical tools and datasets (Price-Whelan 2017) used to study the kinematics of stellar streams and the structural properties of globular clusters (Price-Whelan et al. 2019).

Starting with Gala’s built-in gravitational potential models: we used the spherical Navarro-Frenk-White (Navarro et al. 1996; Navarro et al. 1997, NFW) potential for the dark matter halo, with a circular velocity at the scale radius of 220 km s^{-1} , and a scale radius of 15 kpc. The complete composite model comprises an analytic representation of the bar (Long & Murali 1992), a Miyamoto-Nagai (Miyamoto & Nagai 1975) potential for the galactic disk, with the spherical NFW potential for the halo. The bar was tilted with respect to the x-axis by 25° , with a mass $\frac{1}{6}^{th}$ the mass of the disk component, and the long-axis scale length of the bar was set at 4 kpc. Finally, we assumed that the bar rotates around the z-axis, using a frequency vector: $\Omega = (0, 0, 42) \text{ km s}^{-1} \text{ kpc}^{-1}$.

NGC 6569 was given a current mass of $2.3 \times 10^5 M_\odot$ (Vasiliev & Baumgardt 2021, see Table 1) and modeled by a Plummer potential (Plummer 1911). We experimented with different MW potentials, and found that the details of the tidal debris only differed significantly several degrees away from the current position of the GC, as NGC 6569 is near its apocenter (see Fig.9a for the Galactic xy-plane).

Fardal et al. (2015) described the generation of mock stellar streams: the release of star particles (test particles with no assigned mass) from the cluster. If the globular cluster is not near the pericenter of its orbit, star particles would be “leaking” at some constant rate (unless the orbit was almost circular). Near the pericenter, test particles may be ejected in a “burst”. Since NGC 6569’s orbit is confined to the bulge (See Fig.9), we chose to model the star particle release as a leak at a constant rate of one star particle per 0.5 Myr. This choice was made to plot the location of the current tidal debris that would be located less than a degree from the center of the cluster.

Fig.9 shows the Gala-predicted orbit and the parameter space of the tidal debris (mock stream) of NGC 6569. The top 3 panels (a-c) show the orbit for the previous 250 Myr in the Galactic coordinates, with the present position being the black star. Fig.9d shows the mock stream star particles, color-coded by the RV we would observe in the heliocentric frame. We modeled other local GCs for comparison and found that the thickness of the leading and lagging tidal tails can vary

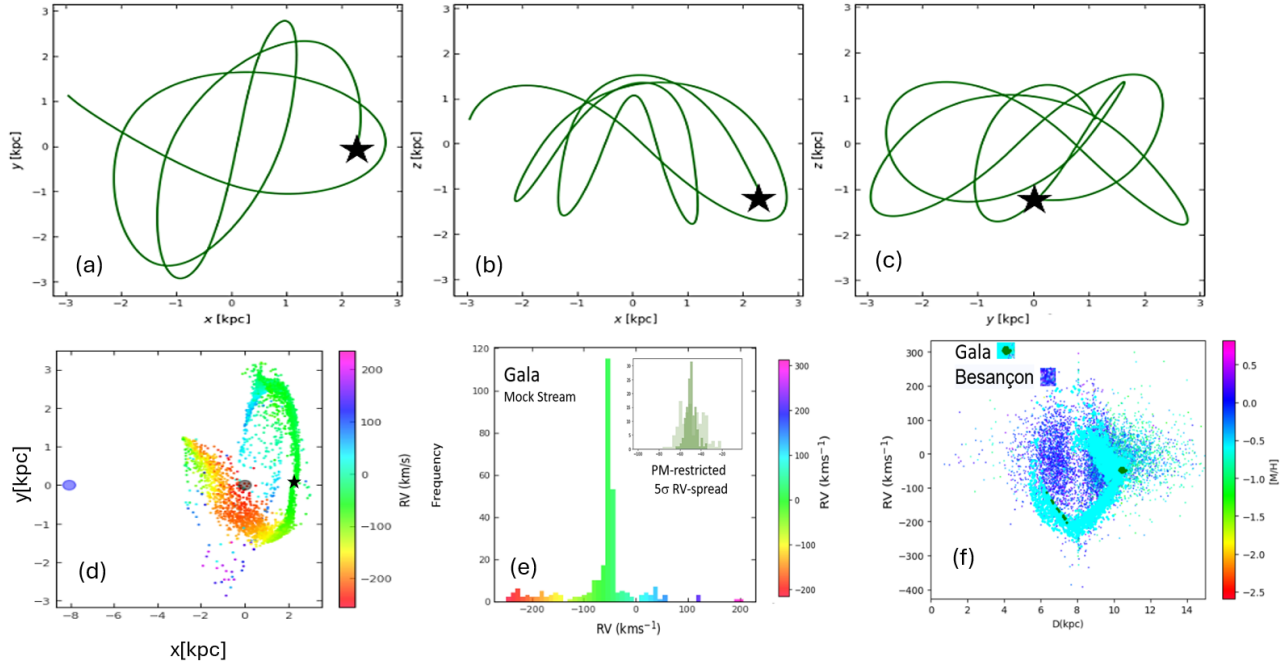


Figure 9. The Gala mock stream models (Price-Whelan 2017) are shown for the orbit of NGC 6569. (a) The orbit of the GC, evolved backward in time for 250 Myr from its current position (shown as a black-filled star) at ~ 2 kpc behind the MW's center. This plot shows the orbit in the x- and y-plane centered on the Galactic Center. (b) The orbit of NGC 6569 for the last 250 Myrs in the x- and z-plane centered on the Galactic Center. (c) The orbit of NGC 6569 for the last 250 Myrs in the y- and z-plane centered on the Galactic Center. (d) Gala-modeled orbit evolved backward in time from the position of the black-filled star for 1 Gyr. Gala's mock stream generator was set to shed a star particle (RV color-coded dots) every 0.5 Myr, using the disk+halo+time-dependent bar potential. A transparent, black-filled circle indicates the Galactic Center, and a transparent, blue-filled circle shows the Sun's position. The RVs are translated back to the heliocentric system observed (color bar, right). This plot shows the orbit in the x- and y-plane centered on the MWGC. (e) The histogram displays the RV for the 4002-star particles, with RVs translated back to the heliocentric frame of reference and color-coded according to the right color bar. We restricted the mock stream to the FOV of our AAT sample and imposed the same PM restrictions on the star particles that were imposed on the AAT sample (olive green inset), where we introduced a 5-standard deviation Gaussian scatter based on the average uncertainty in RV of the AAT/AAOmega spectra (faint olive green in the inset histogram). (f) The whole Gala mock stream is shown in a plot of RV vs. distance in kpc. We color-code the points for metallicity (right side color bar), and show the Besançon model population and the mock stream. Our FOV is shown in green, where most of the stars should be $D > 10$ kpc and $-25 > RV > -65 \text{ km s}^{-1}$, but closer star particles in the bulge are indicated with $-100 > RV > -220 \text{ km s}^{-1}$.

356 depending on several factors, including the cluster's mass and its orbital dynamics. With future
 357 N-body simulations, we will explore the gravitational influences of the surrounding environment.

358 To find the theoretical location of the observable tidal debris around NGC 6569, the Gala code was
 359 executed with negative time steps, using the Gaia DR3 position, PM, and distance, and the catalogued
 360 mass (see Table 1), as initial conditions. The simulation traces NGC 6569 backward to a specified
 361 point in the past, then releases star particles at a user-defined rate moving forward in time as the
 362 cluster orbits through the Galactic bulge. During this process, the test particles are influenced by
 363 the gravitational potential of the progenitor (optional in Gala) and the chosen MW potential. Fig.9d
 364 shows the run for the past 1 Gyr, releasing a star particle every 0.5 Myr for 2000 time steps in the xy-
 365 plane. The dots represent the star particles, color-coded by HRV. Fig.9e shows the absolute number
 366 HRV-histogram of the mock stream star particles. The inset shows our FOV and PM-cut in olive
 367 green, with a simulated spread of 5σ for the average AAOmega spectral uncertainty of $\sim 3 \text{ km s}^{-1}$.
 368 Fig.9f plots this observable RV vs. distance from the solar system (D in kpc), showing the Gala
 369 mock stream in cyan, with our FOV and PM cut in green, overlaying the Besançon models for the
 370 local with our selection parameters. Gala predicts that stars in our field of view should almost all be
 371 from the recent orbit because the GC is near its apocenter, fitting the PM-cut. NGC 6569's current
 372 distance from us is about 10.5 kpc, but it may be possible to detect some stars that escaped earlier
 373 and thus be closer to us ($\sim 6\text{-}8$ kpc).

374 If we took a typical RGB star with $[Fe/H] \approx -0.7$ dex at a distance of ~ 10.5 kpc and adjusted
 375 the distance to 6 kpc, the incorrect luminosity correction to the assumed HB position for the center
 376 of NGC 6569 would return a value $[Fe/H]_{DP} = -1.0$ dex. Such stars would appear brighter than we
 377 assumed, which may be the source of the double HB reported by Mauro et al. (2012), in the K-band,
 378 and suggested by the dereddened BDBS CMDs shown in Fig.1e and Fig.2a. However, the observed
 379 stars with $\Delta[Fe/H] > 0.3$ dex may be variable, causing the discrepancy. Future work will involve
 380 N-body simulations, which will be able to estimate the stellar masses of escaped stars, rather than
 381 just the *massless* mock stream particles.

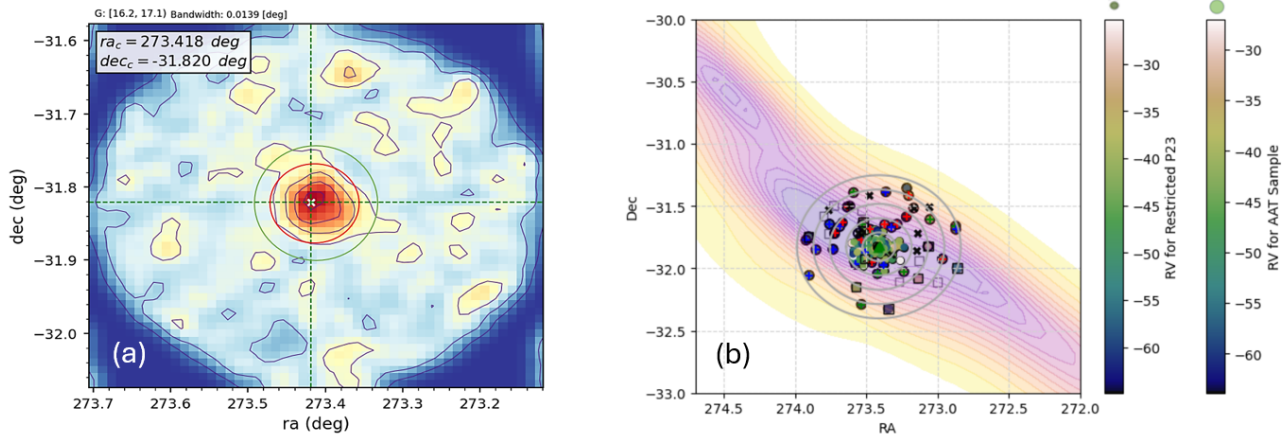


Figure 10. (a) The KDE plot of the NGC 6569 PM-selected Gaia DR3 sample with $17.1 > G > 16.2$ mag. (the HB/RC region, not de-reddened) is shown for a radius of $15'$ around the center of the globular cluster, with north up and east to the left. The average ASteca-determined cluster radius is shown as a red circle, and the tidal radius is shown as a green circle. (b) The Gala mock stream model (Price-Whelan 2017) from Fig.9d is displayed for the orbit of NGC 6569 as the plasma-shaded star-particle density contours, as it would appear on the sky, with R.A. and Dec. (decimal degrees). The open black squares are star particles that may have been released earlier and are near the bulge to our line of sight. The 5 gray circles are 1-5 tidal radii; the largest gray circle is $> 30'$ in radius and corresponds to the FOV shown in Fig.5a. The NGC 6569 AAT sample (58 stars) is shown as large shaded circles, color-coded by the outer right-hand bar. Stars with $-0.5 > [Fe/H]_{SP} > -1.1$ dex are shown as heavy black circles. Extra-tidal candidate A-class stars are shown as green pluses, B-class are the blue pluses, and C-class objects are the red pluses. The RRLs are shown as small, green triangles. The small shaded circles, color-coded by the inner bar, are the published P23 sample. The black open squares are AAT-sample stars with $-220 < RV < -100 \text{ km s}^{-1}$, with $[\alpha/Fe]_{SP} > +0.2$, and $-0.5 > [Fe/H]_{SP} > -1.1$ dex, which the Gala code may identify with part of the mock stream tracing earlier escapees from NGC 6569.

Fig.10 shows how the Gala mock stream compares to the real stars from the AAT sample, and the data sets from P23 and J18. Fig.10a shows a kernel density estimation (KDE) plot for a $15'$ radius around NGC 6569 from the Gaia DR3 database only, selected for the HB/RC region. There are stellar density extensions past the cluster radius (red circle) and tidal radius (green circle), to the NE and SW of the central cluster. Fig.10b shows 1-5 tidal radii circles in gray, superimposed on the KDE plot (plasma shading) of the Gala mock stream. P23's sample of 72 stars (not rejected by RV) yielded 52

objects between $-30 > RV > -63 \text{ km s}^{-1}$ (J18's RV range), which are shown as small shaded circles.
 The black open squares are stars from the AAT data set that may have escaped NGC 6569 on earlier
 orbits that have velocities of -100 to -220 km s^{-1} , but with a similar PM (suggested by Fig.9f). For
 our AAT sample, 50 objects meeting the RV-criteria and $[Fe/H]_{DP}$ limits are marked as black open
 circles, around the shading. We grade the RV-selected extra-tidal candidate stars as ABCD, based on
 matching RV, [Fe/H], and α -abundances (if we can measure them). There are 8 stars within the RV
 range graded F (Table 4), which missed the metallicity cut-off; these are indicated by black crosses.
 There are 7 stars graded A ($-0.5 > [Fe/H]_{SP} > -1.1$ dex, and $[\alpha/\text{Fe}] > +0.2$ dex), shown as large
 bright green plus symbols, also having $\Delta[\text{Fe}/\text{H}] = |[Fe/\text{H}]_{SP} - [Fe/\text{H}]_{DP}| < 0.15$ dex. There are 12
 stars graded B ($-0.5 > [\text{Fe}/\text{H}] > -1.1$ dex and $[\alpha/\text{Fe}] > +0.1$ dex) depicted as small blue plus signs.
 Stars graded C include those with $-0.5 > [\text{Fe}/\text{H}] > -1.1$ dex and $-0.1 < [\alpha/\text{Fe}] < +0.1$ dex, or
 objects with only $[Fe/H]_{DP}$ in the correct range, and are shown as small red plus-signs. Objects with
 $\Delta[\text{Fe}/\text{H}] > 0.30$ dex are represented by small black square borders (grade D), which may indicate
 they are not at the same distance as the main cluster or are variable. RRL stars are marked as green
 triangles in the center of NGC 6569.

Fig.11a is the CMD for the BDBS cluster members from Fig.1e, shown as small gray-filled circles,
 with A-class sources shown as large green plus-signs, B-class are the smaller blue pluses, and C-class
 objects are the small red pluses. F-class objects are shown as black crosses, and D-class stars are
 black open squares. The 10 best ESO spectra are highlighted as yellow squares, and the 4 RRL stars
 are marked as green open triangles (overlapping).

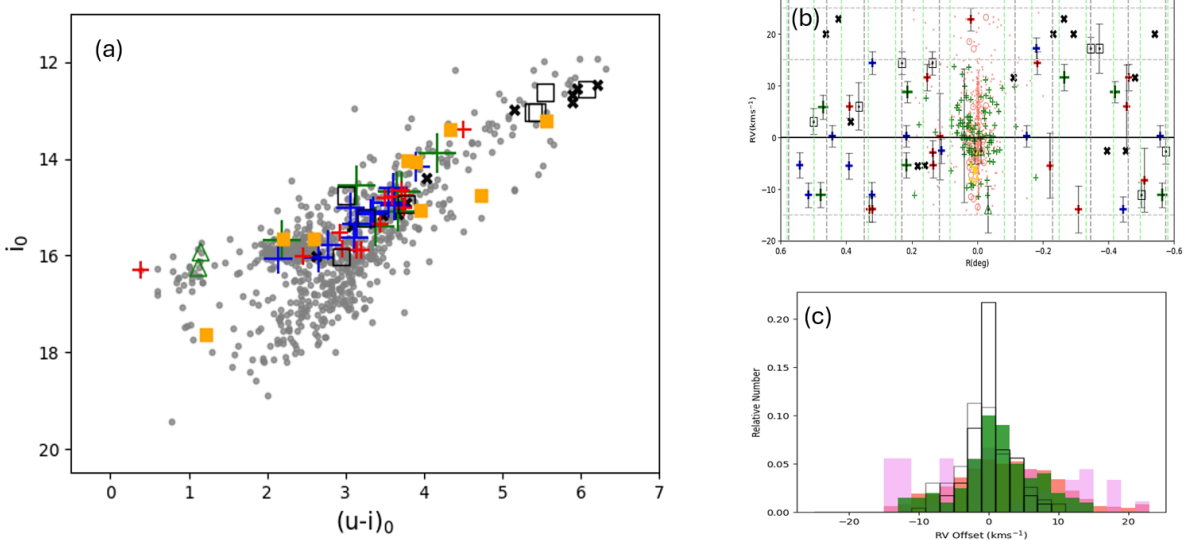


Figure 11. (a) The CMD for the ASteCA-selected cluster members from Fig.1e is shown as small, gray-filled circles. A-class sources are shown as large green plus-signs, B-class are the smaller blue pluses, and C-class objects are the small red pluses. F-class objects are shown as black crosses, and D-class stars are the black open squares. The 10 best ESO spectra are highlighted as yellow squares, and the 4 RRL stars are marked as green open triangles. (b) The normalized radial velocity (RV) offset is plotted against radial distance in degrees on either side of NGC 6569. The tidal radii are indicated in gray for the $6.9'$ or 0.115° tidal radius and light green for the 0.083° tidal radius, calculated using the ASteCA code. From Table 4: 7 stars graded A ($-0.5 > [\text{Fe}/\text{H}]_{SP} > -1.1$ dex, $[\alpha/\text{Fe}] > +0.2$ dex, with $\Delta[\text{Fe}/\text{H}] = |[\text{Fe}/\text{H}]_{SP} - [\text{Fe}/\text{H}]_{DP}| < 0.15$ dex) are shown as large, bright green plus-signs. There are 12 stars graded B ($-0.5 > [\text{Fe}/\text{H}] > -1.1$ dex and $[\alpha/\text{Fe}] > +0.1$ dex) are depicted as small plus signs. Stars graded C include those with $-0.5 > [\text{Fe}/\text{H}] > -1.1$ dex and $-0.1 < [\alpha/\text{Fe}] < +0.1$ dex, or objects with only $[\text{Fe}/\text{H}]_{DP}$ in the correct range, and are shown as small red crosses. Objects with $\Delta[\text{Fe}/\text{H}] > 0.30$ dex are represented by small black open squares (grade D). Stars graded F, with metallicities outside the range $-0.5 > [\text{Fe}/\text{H}]_{DP} > -1.1$ dex, are shown as black crosses. The P23 RV-selected sample is represented by 547 salmon dots, the 45 ESO spectra with $[\text{Fe}/\text{H}]_{SP}$ inside the limits $-0.5 > [\text{Fe}/\text{H}]_{SP} > -1.1$ dex are shown as open salmon circles, and the 10 best ESO spectra highlighted as yellow squares. The J18 sample is depicted with smaller green crosses, and RRL stars are marked as green open triangles. Error bars for the AAT extra-tidal sample are displayed in gray. (c) Relative number histogram of RV offsets: The AAT sample is shown as violet bars, P23's data (547/1073 stars from the paper) is shown as salmon-colored bars, and the J18 sample is displayed as green bars. The Gala mock stream particles are represented by heavy black lines, with the lighter lines indicating the addition of 3 km s^{-1} of random Gaussian noise (approximately 1σ for the AAT data).

408 4. DISCUSSION

409 Tidal stripping can significantly affect the dynamics and evolution of globular clusters, and this
410 process can mimic rotational dynamics within the star clusters. [Piatti \(2020a\)](#) discussed the dis-
411 covery of rotation axis alignments in MW GCs, suggesting that these alignments may influence our
412 understanding of the dynamics within these clusters. Limited rotation signatures could result from
413 the redistribution of stars due to tidal interactions, which can result in the formation of a rotating
414 stellar population as stars are stripped away and the bound stars adjust to the remaining gravita-
415 tional potential. According to P23, their analysis of NGC 6569 indicates that any potential rotational
416 velocity is negligible. Their study involved fitting the density and velocity dispersion profiles of the
417 cluster using non-rotating King models, which suggests that the cluster does not display significant
418 rotational dynamics. [Mauro et al. \(2012\)](#) discusses the characteristics of NGC 6569, noting that
419 while it has a double horizontal branch, there is no indication of significant rotation in its kinematic
420 profile. In this paper, Fig.10d indicates that the faintest and brightest stars in the ‘double-HB’ are
421 separated by only 0.17 dex, which is not statistically significant here, in agreement with J18’s study.

422 Our investigation has revealed that the SP_Ace code is capable of quantifying the abundances of
423 elements other than iron and calcium solely for the brightest stars within this red wavelength range.
424 Consequently, we are unable to utilize these data to distinguish between different generations of stars
425 that are either bound to or escaping from NGC 6569. In contrast, globular clusters such as ω Cen,
426 M22, and NGC 1851 exhibit variations in iron abundance and/or age ([Joo & Lee 2013](#)). Furthermore,
427 even in globular clusters that do not display these signatures, research on multiple stellar populations
428 ([Carretta et al. 2009, 2010](#)) has identified differences in the kinematics between first-generation and
429 second-generation stars, often referred to as populations ([Gratton et al. 2012; Piotto et al. 2015;](#)
430 [Cordoni et al. 2024](#), e.g., 1P and 2P).

431 To ascertain whether the extra-tidal candidates identified by the AAT are first-generation (1P)
432 or second-generation (2P) stars, follow-up observations with higher resolution and signal-to-noise
433 (S/N) ratios are essential. The 2P stars are typically characterized by elevated levels of sodium
434 (Na), nitrogen (N), and helium (He) while exhibiting lower abundances of carbon (C) and oxygen

(O) in comparison to the 1P stars. In a substantial sample of approximately 150 giants from the inner Galaxy, over-abundances of [N/Fe] have been documented, indicating that these stars may have originated in clusters where multiple stellar generations enriched the gas before it was expelled: a comprehensive review can be found in [Milone & Marino \(2022\)](#).

More than 80% of our AAT data set is not moving with NGC 6569. In the AAT sample, 67 objects have $S/N > 35$ or α -abundances that are better than lower limits, but 53 of these stars are not in NGC 6569's RV range (see Fig.8b & d). However, 7 stars outside the RV range of NGC 6569's recently escaped stars have its chemical composition and *could* have escaped earlier (Fig.9d), according to the *Gala* mock stream. Thus, there are 60 stars, orbiting physically close (and in parameter space) to several other bulge GCs, which can be used to study the field population of the bulge, and warrant follow-up spectroscopy to investigate the light element abundances for signatures of formation in GCs. If the metal-poor ($[Fe/H] < -1.1$ dex) field stars in the bulge may have been stripped from GCs ([Schiavon et al. 2017](#); [Fernández-Trincado et al. 2021](#), for example), the simplest explanation for their nitrogen enrichment is that they are remnants of GC populations that were tidally disrupted, possibly leading to the clusters' complete dissolution. Tidal debris from the accreted *Heracles* galaxy remnant ([Horta et al. 2021](#), $M_{Gal} \sim 5 \times 10^5 M_\odot$) has been traced within the inner 4 kpc of the MW, the Sgr Stream has been well-studied, and an extensive list now exists of MW GCs that are suspected of having been accreted from external galaxies, in contrast to those formed *in situ* ([Belokurov & Kravtsov 2023](#)).

5. SUMMARY & CONCLUSIONS

NGC 6569's extra-tidal candidates are classified as follows: 58/303 stars match the original RV-limits, $-25 > RV > -65 \text{ km s}^{-1}$, of which 45 meet the $[Fe/H]_{SP}$ range criteria of $-0.5 > [Fe/H]_{SP} > -1.1$ dex, and 50 stars meet the criteria of $-0.5 > [Fe/H]_{DP} > -1.1$ dex. Some stars were outside the fitting temperature range for the SP_Ace code, but the CaT lines were measurable in 303/305 AAT AAOmega spectra collected for the NGC 6569 field.

Even with magnitude, parallax, and PM cuts, the AStCA photometric results ([Perren et al. 2015](#)) for the combined BDBS and Gaia data yield a contamination index of 0.35 within the cluster's

radius. Either the NGC 6569 stars are too similar to the local field population, or the cluster stars are contaminating the local field. In either case, spectroscopy is necessary to separate any extra-tidal stars being lost by NGC 6569 from the surrounding bulge field population.

This spectroscopic survey shows stars outside the tidal radius selected from the PM, Plx, and CMD isochrone fit (Fig.2b) have a $19 \pm 4\%$ success rate of being in the general RV-range of the cluster. Filtered for the cluster RV, these stars have a $70 \pm 8\%$ chance of having the same broad chemical composition as NGC 6569 stars. Searching the Besançon data shows that 7,562 model stars in our FOV with NGC 6569's PM have a 22% chance of their RVs falling in an acceptable range, which is what we find with our non-uniformly spaced spectroscopic sample. However, there would only be a 7% chance of the Besançon models also having the correct chemical composition, where we find 14% of the AAT sample have both the RV and [Fe/H] values of the cluster. We found that the AAT extra-tidal sample was not statistically different from the Gala model's RV distribution, or those of the cluster members from the J18 and P23 samples. The chemical compositions were also indistinguishable between the on-cluster and off-cluster data sets.

In addition to RV, PM, and chemical composition similarities, NGC 6569's HB/RC population is physically extended along the directions indicated by the Gala mock streams. Both the P23 and J18 data sets fill the ASteCA-derived tidal radius. The J18 sample extends to 0.2° from the cluster center, merging with our AAT extra-tidal sample. Table 4 identifies 41 stars graded ABCD, containing 7 high S/N objects in the group of 19 candidates graded A & B. There are also 4 RRL stars sampled in the center of the cluster. The other candidates (CD) either do not have α -abundances measured or only have [Fe/H] estimated from the CaT lines. Higher resolution spectra of these candidates will be required to make firm judgments on their association with the bound NGC 6569 population.

N-body simulations with modeling of the escaping stars' masses are also desirable to confirm their former membership of NGC 6569. Gala modeling showed where the tidal debris should lie, but this GC's PM and RV are not well-separated from the bulge field stars. Detailed dynamical models are necessary to explore the survival time of NGC 6569, based on its current orbit, trapped within the bulge region.

Table 5. Extra-Tidal Classes & Comparisons

Class	[Fe/H]	$[\alpha/Fe]$	RV	Sample N
Units:	dex	dex	kms^{-1}	
A	-0.86 ± 0.15	$+0.37 \pm 0.06$	-48.9 ± 9.9	7
B	-0.73 ± 0.11	$+0.19 \pm 0.14$	-51.3 ± 9.5	12
C	-0.74 ± 0.12	$+0.13 \pm 0.13$	-50.5 ± 10.9	11
ABCD	-0.76 ± 0.15	$+0.18 \pm 0.14$	-49.0 ± 10.1	40
ESO (Best)	-0.74 ± 0.12	$+0.26 \pm 0.10$	-52.8 ± 5.7	10
ESO (P23)	-0.69 ± 0.24	$+0.26 \pm 0.10$	-50.2 ± 7.6	52
AAT CaT	-0.90 ± 0.34	—	-47.4 ± 9.0	58*
J18 CaT	-0.84 ± 0.17	—	-48.7 ± 5.6	98

NOTE—*Some of this sample are likely closer than 10.5 kpc, making the $[Fe/H]_{DP}$ -values too metal poor due to the erroneous luminosity correction.

489 6. SOFTWARE AND THIRD PARTY DATA REPOSITORY CITATIONS

490 *Software:* astropy, Cloudy, Source Extractor, Scite “Smart Citations”, ChatGPT 4.0, Overleaf

491 *Facilities:* AAT:3.9m, AAVSO, CTIO:1.3m, CTIO:4.0m, CXO

492 The grant support provided, in part, by the M.J. Murdock Charitable Trust (NS-2017321) is acknowledged.
493 Kunder acknowledges support from grant AST-2009836 from the National Science Foundation. This work
494 was made possible through the Preparing for Astrophysics with LSST Program, supported by the Heising-
495 Simons Foundation and managed by Las Cumbres Observatory.

496 This project used data obtained with the Dark Energy Camera (DECam), which was constructed by
497 the Dark Energy Survey (DES) collaboration. Funding for the DES Projects has been provided by the US
498 Department of Energy, the US National Science Foundation, the Ministry of Science and Education of Spain,
499 the Science and Technology Facilities Council of the United Kingdom, the Higher Education Funding Council
500 for England, the National Center for Supercomputing Applications at the University of Illinois at Urbana-
501 Champaign, the Kavli Institute for Cosmological Physics at the University of Chicago, Center for Cosmology
502 and Astro-Particle Physics at the Ohio State University, the Mitchell Institute for Fundamental Physics and
503 Astronomy at Texas A&M University, Financiadora de Estudos e Projetos, Fundação Carlos Chagas Filho
504 de Amparo à Pesquisa do Estado do Rio de Janeiro, Conselho Nacional de Desenvolvimento Científico e
505 Tecnológico and the Ministério da Ciência, Tecnologia e Inovação, the Deutsche Forschungsgemeinschaft
506 and the Collaborating Institutions in the Dark Energy Survey.

507 The Collaborating Institutions are Argonne National Laboratory, the University of California at Santa
508 Cruz, the University of Cambridge, Centro de Investigaciones Enérgéticas, Medioambientales y Tec-
509 nológicas–Madrid, the University of Chicago, University College London, the DES-Brazil Consortium, the
510 University of Edinburgh, the Eidgenössische Technische Hochschule (ETH) Zürich, Fermi National Ac-
511 celerator Laboratory, the University of Illinois at Urbana-Champaign, the Institut de Ciéncies de l’Espai
512 (IEEC/CSIC), the Institut de Física d’Altes Energies, Lawrence Berkeley National Laboratory, the Ludwig-
513 Maximilians Universität München and the associated Excellence Cluster Universe, the University of Michi-
514 gan, NSF’s NOIRLab, the University of Nottingham, the Ohio State University, the OzDES Membership
515 Consortium, the University of Pennsylvania, the University of Portsmouth, SLAC National Accelerator
516 Laboratory, Stanford University, the University of Sussex, and Texas A&M University.

517 This work is based on observations at Cerro Tololo Inter-American Observatory, NSF’s NOIRLab (NOIR-
518 Lab Prop. ID 2013A-0529; 2014A-0480; PI: M. Rich), which is managed by the Association of Universities
519 for Research in Astronomy (AURA) under a cooperative agreement with the National Science Foundation.”

520 This work has made use of data from the European Space Agency (ESA) mission *Gaia* (<https://www.cosmos.esa.int/gaia>), processed by the *Gaia* Data Processing and Analysis Consortium (DPAC, <https://www.cosmos.esa.int/web/gaia/dpac/consortium>). Funding for the DPAC has been provided by national
521 institutions, in particular the institutions participating in the *Gaia* Multilateral Agreement.

REFERENCES

- 524 AAO Software Team 2015, 2dfdr: Data reduction
 525 software, Astrophysics Source Code Library,
 526 record ascl:1505.015 (ascl:1505.015)
- 527 Baumgardt, H. & Hilker, M. 2018, MNRAS, 478,
 528 1520
- 529 Baumgardt, H. & Vasiliev, E. 2021, MNRAS, 505,
 530 5957
- 531 Baumgardt, H., Hénault-Brunet, V., Dickson, N.,
 532 et al. 2023, MNRAS, 521, 3991.
 533 doi:10.1093/mnras/stad631
- 534 Belokurov, V. & Kravtsov, A. 2022, MNRAS, 514,
 535 689. doi:10.1093/mnras/stac1267
- 536 Belokurov, V. & Kravtsov, A. 2023, MNRAS, 525,
 537 4456. doi:10.1093/mnras/stad2241
- 538 Boeche, C. & Grebel, E.K. 2016, A&A, 587 A2
- 539 Boeche, C., Vallenari, A. & Lucatello, S. 2021,
 540 A&A, 645, 35
- 541 Bressan, A., Marigo, P., Girardi, L., et al. 2012,
 542 MNRAS, 427, 127.
 543 doi:10.1111/j.1365-2966.2012.21948.x
- 544 Butler, E., Kunder, A., Prudil, Z., et al. 2024,
 545 ApJL, 963, L33. doi:10.3847/2041-8213/ad20e8
- 546 Carraro, G., Janes, K.A., Eastman, J.D. 2005,
 547 MNRAS, 364, 179
- 548 Carrera, R., Gallart, C., Pancino, E., et al. 2007,
 549 AJ, 134, 1298. doi:10.1086/520803
- 550 Carretta, E., Bragaglia, A., Gratton, R. G., et al.
 551 2009, A&A, 505, 117.
 552 doi:10.1051/0004-6361/200912096
- 553 Carretta, E., Bragaglia, A., Gratton, R. G., et al.
 554 2010, A&A, 516, A55.
 555 doi:10.1051/0004-6361/200913451
- 556 Choi, J., Dotter, A., Conroy, C. et al. 2016, ApJ,
 557 823, 102
- 558 Cole, A. A., Smecker-Hane, T. A., Tolstoy, E., et
 559 al. 2004, MNRAS, 347, 367.
 560 doi:10.1111/j.1365-2966.2004.07223.x
- 561 Cordoni, G., Casagrande, L., Milone, A., et al.
 562 2024, arXiv:2409.02330.
 563 doi:10.48550/arXiv.2409.02330
- 564 Czekaj, M. A., Robin, A. C., Figueras, F., et al.
 565 2014, A&A, 564, A102.
 566 doi:10.1051/0004-6361/201322139
- 567 de Boer, T. J. L., Gieles, M., Balbinot, E., et al.
 568 2019, MNRAS, 485, 4906.
 569 doi:10.1093/mnras/stz651
- 570 Dias, B. & Parisi, M. C. 2020, A&A, 642, A197.
 571 doi:10.1051/0004-6361/202039055
- 572 Dias, B., Palma, T., Minniti, D., et al. 2022,
 573 A&A, 657, A67
- 574 Eisenstein, D.J., Weinberg, D.H., Agol, E. et al.
 575 2011, AJ, 142, 72
- 576 Erkal, D., Koposov, S. E., & Belokurov, V. 2017,
 577 MNRAS, 470, 60. doi:10.1093/mnras/stx1208
- 578 Fardal, M. A., Huang, S., & Weinberg, M. D.
 579 2015, 117 MNRAS, 452, 301
- 580 Ferraro, F. R., Dalessandro, E., Mucciarelli, A., et
 581 al. 2009, Nature, 462, 483.
 582 doi:10.1038/nature08581

- 583 Ferraro, F. R., Massari, D., Dalessandro, E., et al. 615 Horta, D., Mackereth, J. T., Schiavon, R. P., et al.
 584 2016, ApJ, 828, 75. 616 2021, MNRAS, 500, 5462.
 585 doi:10.3847/0004-637X/828/2/75 617 doi:10.1093/mnras/staa3598
 586 Ferraro, F. R., Pallanca, C., Lanzoni, B. et al. 618 Hozumi, S. & Burkert, A. 2015, MNRAS, 446,
 587 2021, Nat. Astron. 5, 311 619 3100. doi:10.1093/mnras/stu2318
 588 Fernández-Trincado, J. G., Beers, T.C., Minniti, 620 Johnson, C. I., Rich, R. M., Caldwell, N., et al.
 589 D. et al. 2021, A&A, 647, 64 621 2018, AJ, 155, 71.
 590 For, B.-Q., Sneden, C., & Preston, G. W. 2011, 622 doi:10.3847/1538-3881/aaa294
 591 ApJS, 197, 29 623 Johnson, C.I., Rich, R. M., Young, M.D. et al.
 592 Gaia Collaboration (Prusti, T., et al.) 2016, A&A, 624 (2020), MNRAS, 499, 2357
 593 595, A1 625 Joo, S.-J. & Lee, Y.-W. 2013, ApJ, 762, 36.
 594 Gaia Collaboration (Brown, A.G.A., et al.) 2021, 626 doi:10.1088/0004-637X/762/1/36
 595 A&A, 649, A1 627 Joyce, M., Johnson, C.I., Marchettie, T., Rich, R.
 596 Gaia Collaboration, 2022, Gaia DR3, Version 1.0. 628 M., Simion, I.T. Bourke, J. et al. (2023), ApJ,
 597 https://doi.org/10.5270/esa-qa4lep3 629 946, 28
 598 Gratton, R. G., Carretta, E., & Bragaglia, A. 630 Kader, J., Pilachowski, C., Johnson, C.I. et al.
 599 2012, A&A Rv, 20, 50. 631 2023, ApJ, 950, 126
 600 doi:10.1007/s00159-012-0050-3 632 King, I. 1962, AJ, 67, 471
 601 Grillmair, C. J. & Dionatos, O. 2006, ApJL, 641, 633 King, I. 1966, AJ, 71, 276
 602 L37. doi:10.1086/503744 634 Koch, A., Xu, S., & Rich, R. M. 2019, A&A, 627,
 603 Grocholski, A. J. 2006, Ph.D. Thesis 635 A70. doi:10.1051/0004-6361/201935467
 604 Grocholski, A. J., Sarajedini, A., Olsen, K. A. G., 636 Kroupa, P. 2002, Science, 295, 82.
 605 et al. 2007, AJ, 134, 680. doi:10.1086/519735 637 doi:10.1126/science.1067524
 606 Grondin, S. M., Webb, J. J., Leigh, N. W. C., 638 Kunder, A., Kordopatis, G., Steinmetz, M. et al.
 607 Speagle, J. S., Khalifeh, R. J. 2023, MNRAS, 639 2017, AJ, 153, 75
 608 518, 4249 640 Kunder, A., Stetson, P. B., Catelan, M., et al.
 609 Harris, W. E. 1996, AJ, 112, 1487. 641 2015, Fifty Years of Wide Field Studies in the
 610 doi:10.1086/118116 642 Southern Hemisphere: Resolved Stellar
 611 Harris, W. E. 2010, arXiv:1012.3224. 643 Populations of the Galactic Bulge and
 612 doi:10.48550/arXiv.1012.3224 644 Magellanic Clouds, 491, 104
 613 Hazen-Liller, M. L. 1985, AJ, 90, 1807. 645 Kunder, A., Prudil, Z., Covey, K. R., et al. 2024,
 614 doi:10.1086/113881 646 AJ, 167, 21. doi:10.3847/1538-3881/ad0cfcc

- 647 Kurtz, M. J., Mink, D. J., Wyatt, W. F., et al.
 648 1992, Astronomical Data Analysis Software and
 649 Systems I, 25, 432
- 650 Lim, D., Lee, Y.-W., Koch, A., Hong, S., Johnson,
 651 C. I., Kim, J., Chung, C., Mateo, M., Bailey,
 652 J.I. 2021, ApJ, 907, 47
- 653 Long, K. & Murali, C. 1992, ApJ, 397, 44
- 654 Mauro, F., Moni Bidin, C., Cohen, R., et al. 2012,
 655 ApJL, 761, L29.
 656 doi:10.1088/2041-8205/761/2/L29
- 657 Milone, A. P. & Marino, A. F. 2022, Universe, 8,
 658 359. doi:10.3390/universe8070359
- 659 Minniti, D., Lucas, P. W., Emerson, J. P., et al.
 660 2010, NewA, 15, 433.
 661 doi:10.1016/j.newast.2009.12.002
- 662 Minniti, D., Fernández-Trincado, J.G., Ripepi, V.,
 663 Alonso-García, J., Contreras Ramos, R.,
 664 Marconi, M. 2018, ApJ, 869, 10
- 665 Miyamoto M. & Nagai R., 1975, Pub. Astron.
 666 Soc. Japan 27, 533
- 667 Moreno, E., Pichardo, B. & Velázquez, H. ApJ,
 668 793, 2
- 669 Navarro, J. F., Frenk, C. S., & White, S. D. M.
 670 1996, ApJ, 462, 563. doi:10.1086/177173
- 671 Navarro, J.F., Frenk, C.S., White, S.D.M. 1997,
 672 ApJ, 490, 493
- 673 Odenkirchen, M., Grebel, E. K., Rockosi, C. M., et
 674 al. 2001, ApJL, 548, L165. doi:10.1086/319095
- 675 Odenkirchen, M., Grebel, E. K., Dehnen, W., et
 676 al. 2003, AJ, 126, 2385. doi:10.1086/378601
- 677 Ortolani, S., Bica, E., & Barbuy, B. 2001, A&A,
 678 374, 564. doi:10.1051/0004-6361:20010753
- 679 Pallanca, C., Leanza, S., Ferraro, F. R., et al.
 680 2023, ApJ, 950, 138.
 681 doi:10.3847/1538-4357/accce9
- 682 Parisi, M.C., Gramajo, L.V., Geisler, D. et al.
 683 2022, A&A, 662, A75
- 684 Perren, G. I., Vázquez, R. A., Piatti, A. E. 2015,
 685 A&A, 576, 6
- 686 Perren, G. I., Pera, M. S., Giorgi, E. E., et al.
 687 2022, Boletin de la Asociacion Argentina de
 688 Astronomia La Plata Argentina, 63, 124
- 689 Piatti, A. E. 2020, A&A, 638, L12.
 690 doi:10.1051/0004-6361/202038494
- 691 Piatti, A. E. & Carballo-Bello, J. A. 2020, A&A,
 692 637, L2. doi:10.1051/0004-6361/202037994
- 693 Piatti, A. E. 2024, AJ, 167, 279.
 694 doi:10.3847/1538-3881/ad4704
- 695 Piatti, A. E. 2024, A&A, 683, A151.
 696 doi:10.1051/0004-6361/202348534
- 697 Piotto, G., Milone, A. P., Bedin, L. R., et al. 2015,
 698 AJ, 149, 91. doi:10.1088/0004-6256/149/3/91
- 699 Plummer, H. C. 1911, MNRAS, 71, 460
- 700 Pritzl, B., Smith, H. A., Catelan, M., & Sweigart,
 701 A. V. 2000, ApJ, 530, 41
- 702 Pritzl, B., Smith, H. A., Catelan, M., & Sweigart,
 703 A. V. 2001, AJ, 122, 2600
- 704 Price-Whelan, A. M., Sesar, B., Johnston, K.V.,
 705 Rix, H.-W. 2016, ApJ, 824, 104
- 706 Price-Whelan, A. M. 2017, The Journal of Open
 707 Source 134 Software, 2, 388, doi:
 708 10.21105/joss.00388

- 709 Price-Whelan, A. M., Mateu, C., Iorio, G., et al.
710 2019, AJ, 158, 223.
711 doi:10.3847/1538-3881/ab4cef
- 712 Price-Whelan, A., Sipo"cz, B., Starkman, N., et
713 al. 2022, 131 adrn/gala: v1.5, v1.5, Zenodo,
714 Zenodo, 132 doi: 10.5281/zenodo.6325733
- 715 Ramos, P., Antoja, T., Yuan, Z., et al. 2022,
716 VizieR Online Data Catalog, 366
- 717 Rich, R. M., Johnson, C. I., Young, M. et al. 2020,
718 MNRAS, 499, 2340
- 719 Robin, A. C. 2012, European Physical Journal
720 Web of Conferences, 19, 09003.
721 doi:10.1051/epjconf/20121909003
- 722 Saracino, S., Dalessandro, E., Ferraro, F. R., et al.
723 2019, ApJ, 874, 86.
724 doi:10.3847/1538-4357/ab07c4
- 725 Schiavon, R. P., Zamora, O., Carrera, R., et al.
726 2017, MNRAS, 465, 501
- 727 Simion, I. T., Belokurov, V., Irwin, M., et al.
728 2017, MNRAS, 471, 4323
- 729 Sneden, C., Preston, G. W., Chadid, M., &
730 Adamów, M. 2017, ApJ, 848, 68
- 731 Steinmetz, M., Guillaume, G., McMillan, P.J.
732 et al. 2020, AJ, 160, 83
- 733 Tinsley, B. M. 1979, ApJ, 229, 1046.
734 https://doi.org/10.1086/157039
- 735 Valenti, E., Origlia, L., & Ferraro, F. R. 2005,
736 MNRAS, 361, 272.
737 doi:10.1111/j.1365-2966.2005.09173.x
- 738 Valenti, E., Origlia, L., & Rich, R. M. 2011,
739 MNRAS, 414, 2690.
740 doi:10.1111/j.1365-2966.2011.18580.x
- 741 Vasiliev, E. 2018, Astrophysics Source Code
742 Library. ascl:1805.008
- 743 Vasiliev, E., & Baumgardt, H. 2021, MNRAS,
744 505, 5978
- 745 Wallerstein, G. 1962, The Astrophysical Journal
746 Supplement Series, 6, 407.
747 https://doi.org/10.1086/190067
- 748 Zhang, S., Mackey, D., & Da Costa, G. S. 2022,
749 MNRAS, 513, 3136. doi:10.1093/mnras/stac751